Research paper

Burial evolution of evaporites with implications for sublacustrine fan reservoir quality: A case study from the Eocene Es4x interval, Dongying depression, Bohai Bay Basin, China

Benben Ma [a, b], Yingchang Cao [a, **], Kenneth A. Eriksson [b, *], Yancong Jia [c], Yanzhong Wang [a]

[a] School of Geosciences, China University of Petroleum, Qingdao, 266580, China
[b] Department of Geosciences, Virginia Tech, Blacksburg, VA 24061, United States
[c] School of Energy, China University of Geosciences, Beijing, 100083, China

ARTICLE INFO

ABSTRACT

Eocene, sublacustrine-fan, sandstones that developed in a rift basin are important tight gas reservoirs in the Dongying Depression, Bohai Bay Basin, northeastern China. Two units of evaporites, developed at the top and bottom of the lower unit of the Es4 interval (Es4x), consist predominantly of anhydrite with subordinate gypsum. Evaporite and related diagenetic processes greatly influenced reservoir quality. $\delta^{13}C$ values for micritic dolomite cements in Es4x are depleted (-7.45 to -2.57‰) due to microbial sulfate reduction (MSR) under shallow burial conditions and this interpretation is supported by large $\delta^{34}S$ fractionation between anhydrite and framboidal pyrite. Precipitation temperatures for micritic dolomite are calculated as $57.5-72.8$ °C. Anhydritization of gypsum probably occurred at $100.5-145.2$ °C during progressive burial as evidenced by homogenization temperatures of aqueous inclusions within anhydrite cements. This process resulted in dehydration fractures within anhydrite cements that increased reservoir permeability by connecting isolated pores. Thermochemical sulfate reduction (TSR) probably resulted in dissolution of gypsum and anhydrite cements under relatively deep burial conditions. Ankerite cements are replaced by anhydrite cements and are enclosed by solid bitumen in Es4x. Ankerite cements likely were derived from TSR as reflected in negative $\delta^{13}C$ values (-7.12 to -3.70‰) and high calculated temperatures ($121.3-185.1$ °C). Dissolution by-products (e.g. saddle dolomite, ankerite, nodular pyrite) related to TSR precipitated in adjacent pores. A lack of significant $\delta^{34}S$ fractionation between parent sulfate and nodular pyrite indicates that TSR occurred in a relatively closed system. Therefore, dissolution of gypsum and anhydrite related to TSR contributed little to reservoir quality. Middle-fan lithofacies with better sorting, porosity and permeability than inner- and outer-fan lithofacies constitute high-quality reservoirs in Es4x.

© 2016 Elsevier Ltd. All rights reserved.

1. Introduction

Evaporites have been studied broadly in different basins worldwide, mainly in relation to tectonic setting (e.g. Ortí et al., 2014; Schorn and Neubauer, 2014), depositional environments (e.g. Taberner et al., 2000; Trichet et al., 2001; Topper and Meijer, 2013), sequence stratigraphy (e.g. Tucker, 1991; Sarg, 2001) and mineralogy and geochemistry (e.g. Bahadori et al., 2011; Iribar and

Ábalos, 2011; Tangestani and Validabadi, 2014). Evaporites typically develop in semi-arid or arid climatic settings where evaporation exceeds precipitation (Sarg, 2001; Trichet et al., 2001; Warren, 2006) and are closely associated with carbonate rocks (e.g. Major and Holtz, 1997; Tanguay and Friedman, 2001). Diagenesis of evaporites and related diagenetic processes (e.g. carbonate cementation) have been shown to exert a critical influence on reservoir quality (e.g. Machel and Buschkuehle, 2008; Rahimpour-Bonab et al., 2010).

Transformation of gypsum to anhydrite with progressive burial has been related to increases in temperature (95–200 °C) and pressure (0–100 MPa), and the geochemistry of pore fluids (saline

* Corresponding author.
** Corresponding author.
E-mail addresses: cyc8391680@163.com (Y. Cao), kaeson@vt.edu (K.A. Eriksson).

to hypersaline brines) (e.g. Jowett et al., 1993; Ogawa et al., 2007; Amadi et al., 2012). Changes in pore fluid compositions with burial, in turn, influence later diagenesis (e.g. Nollet et al., 2005; Amadi et al., 2012). Moreover, gypsum and anhydrite are readily dissolved in the presence of hydrocarbons and acidic solutions (e.g. Baruah et al., 2000; Bildstein et al., 2001). Gypsum/anhydrite can react with hydrocarbons and result in dissolution associated with thermochemical sulfate reduction (TSR) at elevated temperatures (Worden et al., 2000; Machel, 2001; Hao et al., 2015). Dissolution of gypsum/anhydrite during TSR and its influence on reservoir quality are equivocal with ongoing debates focusing on whether dissolution by-products are removed from the system or precipitated *in-situ* (Machel, 2001; Hao et al., 2015).

The Eocene Es4 (Es4s and Es4x) interval in the Dongying Depression, Bohai Bay Basin in eastern China (Fig. 1) developed in a rift basin. Evaporites in the form of anhydrite and gypsum, and dark mudstones and deep-water sublacustrine fan facies are present at burial depths of 4000–5000 m in the lower unit (Es4x) (Fig. 2). Conversion of gypsum to anhydrite resulted in modification of the composition of pore fluids but this process is complicated at elevated temperatures and pressures, and is greatly influenced by the composition of deep burial brines (Jowett et al., 1993; Amadi et al., 2012). With a range of burial depths (4000–5000 m), formation temperatures (150–200 °C) and formation pressures (40–70 Mpa), the Es4x in Dongying Depression is ideally suited to investigate the burial evolution of evaporites and their influence on reservoir quality. Thus, the objectives of this study are to: (1) document the distribution of evaporitic minerals such as gypsum, anhydrite and halite using thin section petrography in combination with a range of analytical techniques; (2) understand diagenetic alterations of evaporites and associated minerals by utilizing fluid inclusion and stable isotope data; (3) illustrate that evaporite transformation resulted in dehydration fractures that influenced reservoir quality; and (4) evaluate the effects of evaporite transformation (gypsum to anhydrite) and dissolution on the diagenesis and, thereby, the reservoir quality of associated sandstones. Formation of dehydration fractures within anhydrite cements associated with anhydritization of gypsum has not been documented in previous research whereas the effects of gypsum and anhydrite dissolution (related to thermochemical sulfate reduction) on associated sandstone reservoirs has not been evaluated within the study area (e.g. Yuan and Wang, 2001; Chen et al., 2013). Sublacustrine fan deposits with associated evaporites are widely developed in eastern China (e.g. Guo et al., 2010; Jiang et al., 2013) and worldwide (e.g. Schenk et al., 1994; Warren, 2010) and, therefore, the results of this study have wide application to lacustrine reservoirs of similar tectono-sedimentary and diagenetic origin.

2. Geological setting

The Dongying Depression is located in the southern part of the Jiyang Subbasin of the Bohai Bay Basin (Yuan and Wang, 2001; Guo et al., 2010) and covers an area of 5700 km^2 (Fig. 1A, B). Tectonic evolution of the depression is characterized by a syn-rift stage between 65.0 and 24.6 Ma and a post-rift stage from 24.6 Ma to the present (Hu et al., 2001; Guo et al., 2010; Dong et al., 2011). The Dongying Depression consists of five secondary tectonic units from north to south: the northern steep slope, the northern sag (Minfeng Sag), the central anticline, the southern sag (Niuzhang Sag), and the southern gentle slope (Fig. 1C). The Minfeng Sag is located in the northeastern part of the Dongying Depression and the northern margin of the sag is defined by the Chennan Boundary Fault (Fig. 1C; Jiang et al., 2013).

Stratigraphic successions in the Dongying Depression consist of the Paleocene Kongdian (Ek), Shahejie (Es), and Dongying (Ed) formations, the Neogene Guantao (Ng) and Minghuazhen (Nm) formations, and the Quaternary Pingyuan (Qp) Formation (Fig. 3). The Eocene Es4x interval is an important tight gas reservoir in the Dongying Depression and is the subject of this study (Fig. 2; Wan et al., 2010; Wang et al., 2014). Es4x consists of dark lacustrine source rocks, evaporites interbedded with multi-stage, sublacustrine fan sandy conglomerates, pebbly sandstones and sandstones close to the boundary fault (Fig. 2). Evaporites in cumulative thicknesses of more than 1600 m are located at the bottom and the top of Es4x (Fig. 2).

During the initial deposition of Es4x, lake water had relatively high salinity associated with arid climatic conditions that resulted in the precipitation of gypsum and subordinate halite (Song et al., 2009; Wang et al., 2014). For most of the time of Es4x deposition, seasonal floods carried abundant siliciclastic sediments into the lake and large, sublacustrine fans developed adjacent to the footwall of the Chennan Boundary Fault and interfingered with more distal mudstones (Fig. 2). A return to arid conditions late in the history of Es4x deposition resulted in a second stage of evaporite precipitation. Multi-stage sublacustrine fan deposits are overall retrogradational and onlap the boundary fault (Fig. 2); this pattern is attributed to a long-term rise in lake level (Song et al., 2012).

Sublacustrine-fan deposits can be subdivided into inner-fan, middle-fan and outer-fan facies based on analysis of lithologies and sedimentary structures (Fig. 4; Sui et al., 2010; Cao et al., 2014; Wang et al., 2014). Matrix- or framework-supported conglomerates (Fig. 5A) are interpreted as inner-fan deposits that developed on steep slopes adjacent to the boundary fault (Fig. 4). Coarse-grained pebbly sandstones (Fig. 5B) and medium- or coarse-grained sandstones developed in braided channel in the middle-fan on relatively gentle slopes (Fig. 4). Graded, thin-bedded siltstone or fine-grained sandstones (Fig. 5C) were deposited in interdistributary areas in the middle-fan and on outer-fan (Fig. 4) and grade basinwards into deep lacustrine mudstones (Fig. 5D). Evaporites in Es4x (Fig. 5E) are interbedded with dark mudstones (Fig. 5F). Locally, evaporites (mainly anhydrite) are impregnated with oil (Fig. 5E) and fill fractures in mudstones (Fig. 5F).

3. Samples and methods

Core samples were collected from eight boreholes in the Eocene Es4x at depths ranging from 4000 to 5000 m (Fig. 4). Fifty three (53) thin sections, impregnated with pink epoxy under vacuum and stained with alizarin red-S and potassium ferricyanide (Dickson, 1965), were prepared for determining rock compositions, diagenetic constituents and percentages and types of porosity. Percentages of framework grains, authigenic cements and porosity were determined by 400 point counts per thin section.

Twelve (12) gold-coated sample chips were prepared for determining the compositions of authigenic minerals and spatial relationships, using a JSM-5500LV scanning electron microscope (SEM) equipped with a QUANTAX 400 energy dispersive X-ray spectra (EDX) under an acceleration voltage of 20 kV using a beam current of 1.0–1.5 nA. Highly magnified backscatter (BSE) and secondary electron (SE) techniques were used to determine the compositions of zoned carbonate cements. X-ray spectrometry was used to generate element distribution maps and for quantitative point analyses to further characterise the compositions of carbonate and evaporite cements. X-ray diffraction (XRD) analysis using an Ultima IV X-ray diffractometer at the Exploration and Development Research Institute of the Sinopec Zhongyuan Oilfield Company was carried out on <10 μm, air-dried powders to determine the compositions of whole rocks.

Eleven (11) samples from six boreholes were prepared for
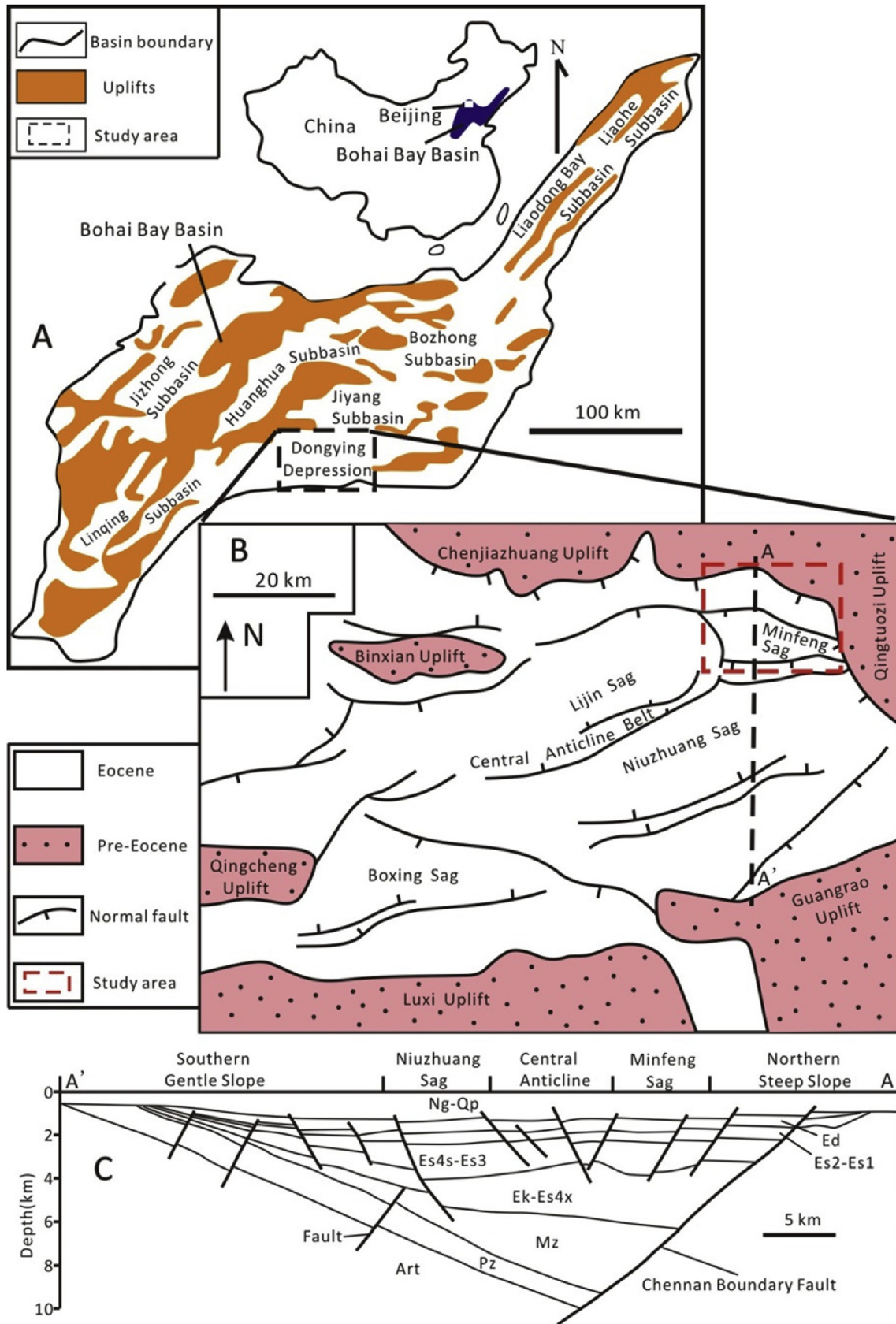
Fig. 1. (A) Locality map of subbasins of the Bohai Bay Basin, eastern China (modified from Guo et al., 2010); (B) Distribution of main sags and uplifts and major faults and location of section AA′; (C) Cross section AA′ showing major stratigraphic units and major tectonic features within the Dongying depression (modified from Guo et al., 2010).
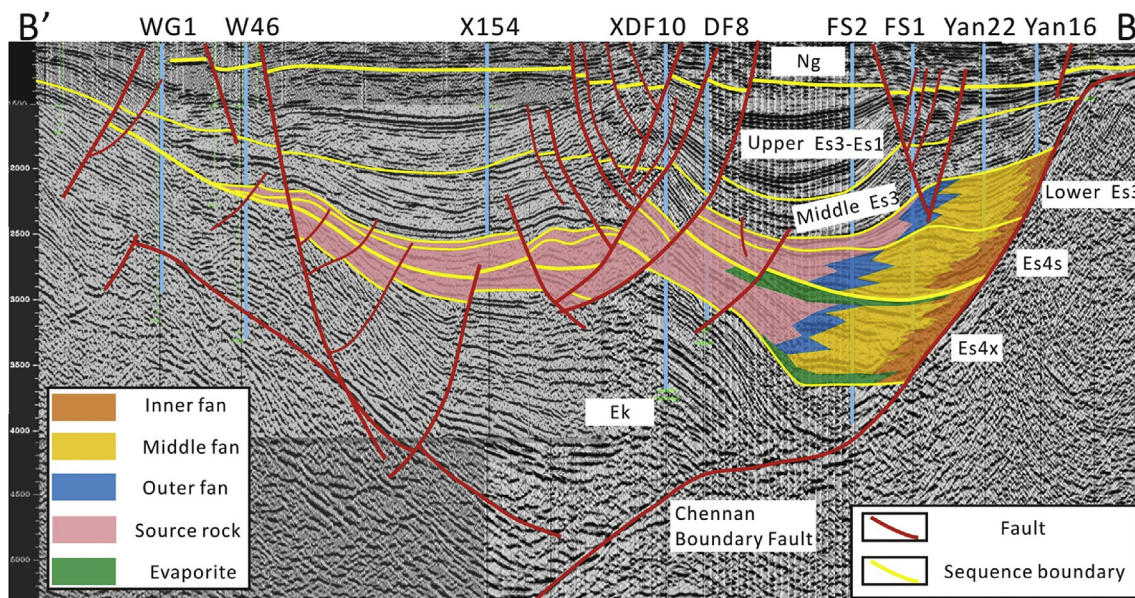
Fig. 2. Interpreted seismic cross section through the study area showing lithologies in Es4x and major extensional faults.
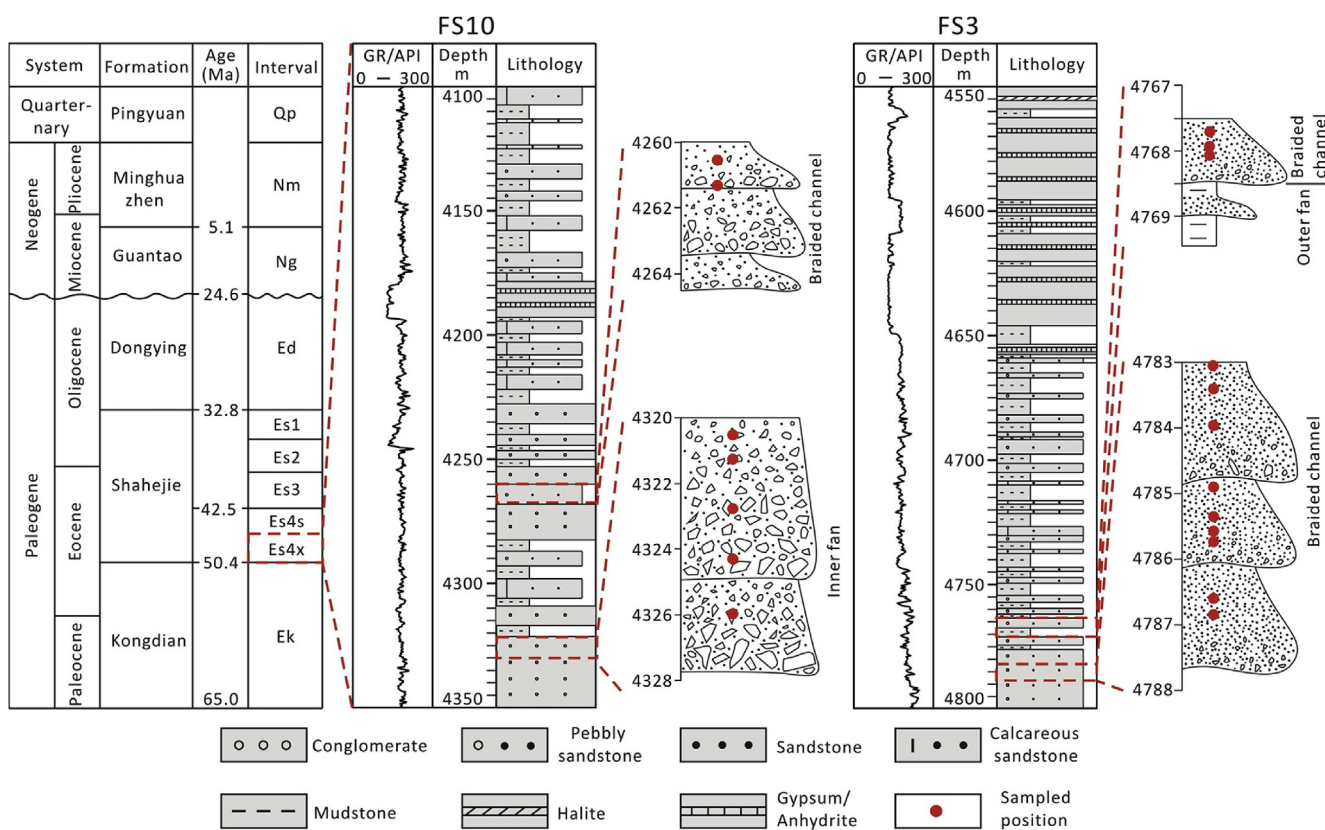
Fig. 3. Tertiary stratigraphy of the Dongying depression and lithologic columns of the various lithofacies in Es4x.

carbon and oxygen isotope analyses. In order to avoid sample contamination, microsamples (0.35–0.45 mg) of different pure carbonate cements were drilled from thick petrographic and stained sections using a microscope-mounted dental drill. Each sample was reacted with 100% ortho-phosphoric acid at 70 °C for 4–8 h. Carbon and oxygen isotope data were obtained by measuring the CO_2 gas produced by acidification of the sample.

Samples were measured on an Isoprime 100 isotope-ratio mass spectrometer (IRMS) coupled with a peripheral MultiFlow-Geo headspace sampler in the Stable Isotope Facility in the Department of Geosciences at Virginia Polytechnic Institute and State University. Carbon and oxygen isotope compositions are reported in standard delta notation as per mil (‰) deviations from Vienna Pee Dee Belemnite (VPDB). Replicated measurements of the
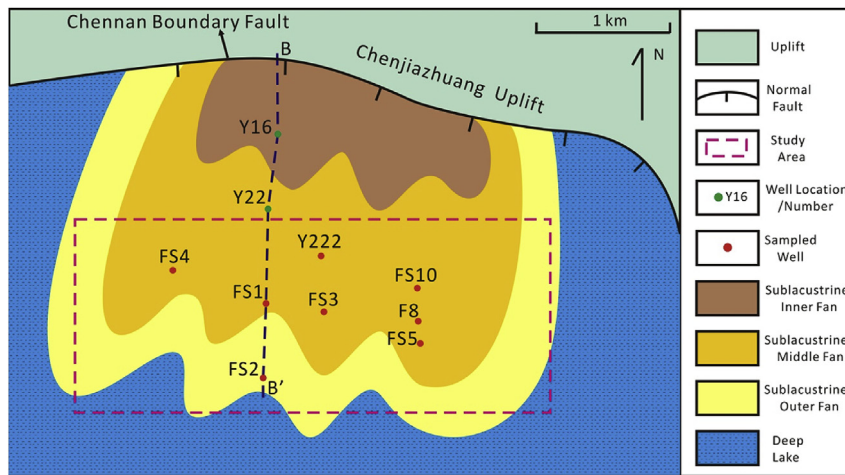
Fig. 4. Map of facies with well locations referred to in the text and location of section BB' (Fig. 2) in the northern Minfeng sag, Dongying depression.
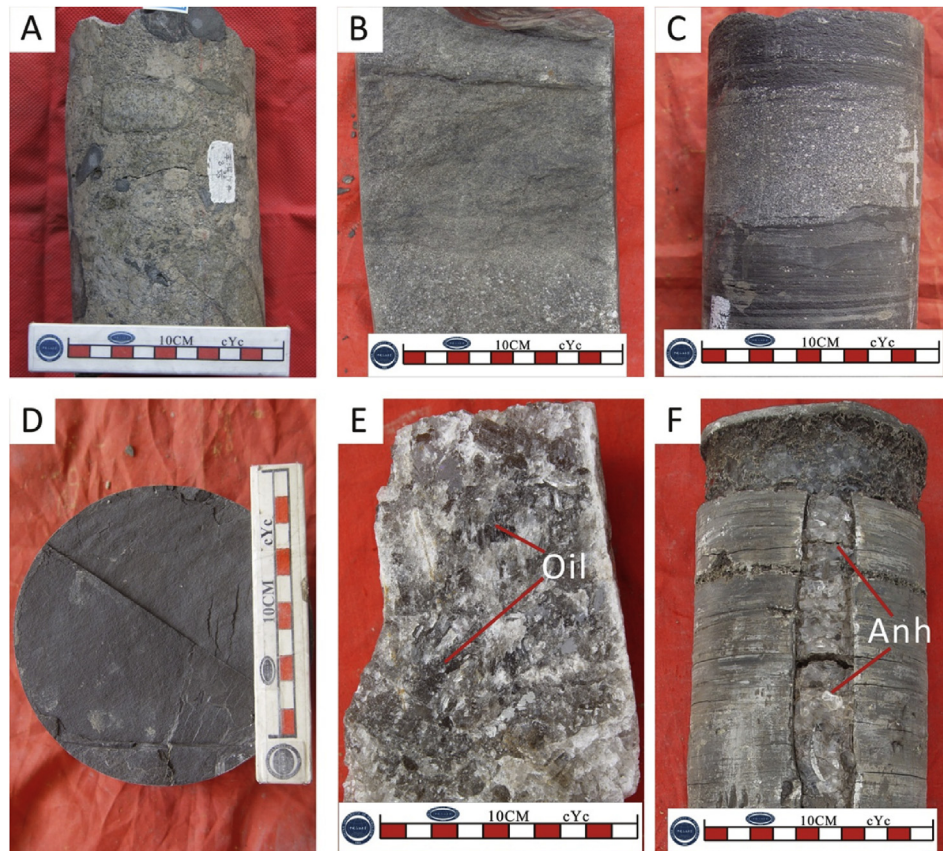
Fig. 5. Photographs of lithofacies in Es4x. (A) Conglomerate: inner-fan, Well FS10, 4326.7 m; (B) Coarse-grained pebble sandstone: middle-fan, Well FS3, 4786.4 m; (C) Fine-grained sandstone interbedded with thick mudstone: outer-fan, Well FS10, 3923.4 m; (D) Dark mudstone, Well FS2, 4300.2 m; (E) Evaporite with oil impregnation, Well FS2, 5580.4 m; (F) Evaporites interbedded with mudstones and mudstone fractures filled with evaporites, Well FS2, 4300.7 m. Anh = Anhydrite.

International Atomic Agency Standards (IAEA) CO-1, CO-9 and NBS-18 standards were ±0.04‰ for $\delta^{13}C$, and ±0.18‰ for $\delta^{18}O$ ±0.2‰ (1σ).

Eight (8) anhydrite- and pyrite-cemented samples from five boreholes were prepared for sulfur isotope analysis. Samples were collected using a handheld dremel tool and approximately 0.1 g of powder was generated from each sample. Powders were reacted with a 1.7 M NaCl solution for approximately 48 h to dissolve

anhydrite from the sample. Samples were then centrifuged and the solution and residual solid were separated. A 1 M $BaSO_4$ solution was added to solutions to precipitate sulfate as $BaSO_4$. The $BaSO_4$ was dried and 0.350−0.400 mg per sample was loaded into tin capsules with excess V_2O_5. The residual solid was dried and loaded into tin capsules with excess V_2O_5 for pyrite sulfur isotope analysis. Sulfur isotopic analyses were performed with an Elementar Vario ISOTOPE Cube elemental analyzer connected to an Isoprime 100

isotope ratio mass spectrometer in the Stable Isotope Facility in the Department of Geosciences at Virginia Polytechnic Institute and State University. Sulfur isotope compositions are reported in standard delta notation as per mil (‰) deviations from Vienna Canon Diablo Troilite (VCDT). For the sulfate sulfur isotope measurements, replicated analyses of IAEA-SO-5, SO-6 and NBS-127 standards during sample analyses were ±0.2‰ or better (1σ). For the pyrite sulfur isotope measurements, replicated analyses of IAEA-S-1, S-2 and S-3 during sample analyses were ±0.2‰ or better (1σ).

Fluid inclusions within anhydrite cements were studied on five doubly polished thick sections (approximately 100 μm) using a LINKAM THMSG600 heating-freezing stage. Petrography of fluid inclusions was conducted using a Zeiss Axio Scope A1 microscope. Special attention was paid to identifying fluid inclusion assemblages (FIAs) that represent the most finely discriminated groups of petrographically associated inclusions of fluids that were trapped at the same time (Goldstein and Reynolds, 1994). The thick sections were cut into small chips and target FIAs observed in each chip were selected for microthermometric measurements. The homogenization temperature (Th) was measured using a heating rate of 10 °C/min for temperatures less than 80 °C and a rate of 5 °C/min for temperatures exceeding 80 °C. Homogenization temperatures were obtained by cycling (Goldstein and Reynolds, 1994). Precision for Th measurements is±1 °C and for ice final melting temperature (Tm) is ±0.1 °C. Salinities were calculated from Tm based on the revised equation of Bodnar (1993) for NaCl–H$_2$O solutions.

Plug porosity and permeability were determined based on 73 cylindrical core samples (diameter = 25 mm, length = 30–40 mm) at depths of 4000–5000 m from six boreholes at the Exploration and Development Research Institute of the Sinopec Zhongyuan Oilfield Company. The gas expansion method was used for determining porosity and helium was used as the measuring medium. The pressure-transient technique was adopted for measuring permeability in a gas-autoclave (Siriwardane et al., 2009; Rahman and McCann, 2012) and nitrogen was used as the permeating medium. In addition, the presence or absence of hydrocarbons was observed in 73 plug samples, and determined quantitatively by down-well measurements using density, sonic and neutron logs.

4. Framework petrology

Sandstones in Es4x are mostly coarse-grained and moderately to poorly sorted and are predominantly lithic arkoses and feldspathic litharenites (Fig. 6). Based on point counting (Supplementary Material 1), feldspar is the most common framework grain including K-feldspar and plagioclase and ranges in abundance from 25% to 55% (ave. 40.9%). Detrital K-feldspar (15–35%, ave. 23.7%) is more abundant than plagioclase (8–25%, ave. 16.2%). Rock fragments (15–56%, ave. 32.3%) are dominated by sedimentary lithics (mainly dolomite and limestone). Quartz is the least common framework grain (12–50%, ave. 26.8%).

5. Characteristics of diagenetic minerals

5.1. Gypsum and anhydrite cements

Gypsum and anhydrite beds as well as cements are pervasively developed in Es4x. Anhydrite (0.1%–12.0%) and subordinate gypsum (0.2–3.5%) cements in sandstones normally occur as elongated lath-shaped (Fig. 7A, B; Supplementary Material 1) and pore-filling, blocky crystals (Fig. 7C, D). X-ray diffraction analysis confirms the presence of gypsum and anhydrite at depths greater than 4 km and indicates that anhydrite is more abundant than gypsum at these depths (Fig. 8). Comparable occurrences of gypsum and anhydrite developed at burial depths of ~4 km have been reported in the
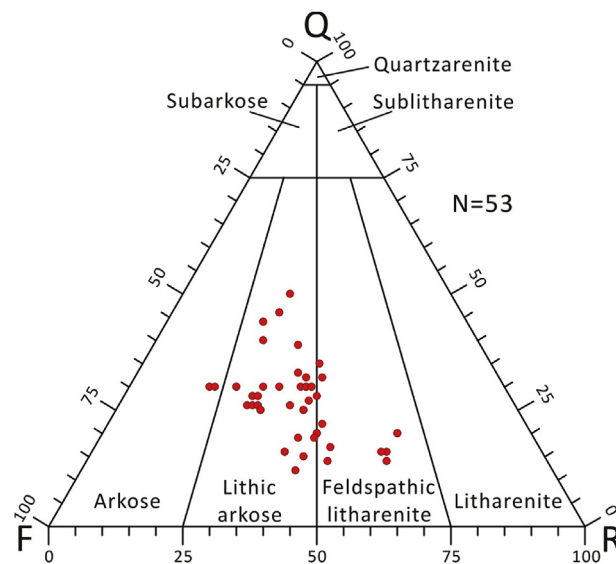
Fig. 6. Ternary plot of point count data on a base of Folk (1974).

Mississippi Interior Salt Basin (Amadi et al., 2012). Commonly, gypsum is replaced by anhydrite with the same preferred orientation and gypsum pseudomorphs are well preserved in the anhydrite laths (Fig. 7A). SEM images confirm the presence of lath-shaped anhydrite crystals (Fig. 7E). Gypsum and anhydrite cements are closely associated with and engulfed by micritic dolomite (Fig. 7C). Locally, blocky anhydrite occurs as micro-fracture filling cements in mudstone (Fig. 5F). Anhydrite cements commonly are replaced by ankerite (Fig. 7D). Abundances of gypsum and anhydrite are not linearly correlated with burial depth but both occur in highest abundances at approximate depths of 4300–4500 m (Fig. 9A, B).

5.2. Halite

Halite (trace to 1.0%) occurs locally in the form of cubic microcrystals (<5 μm) within pores in sandstones (Fig. 7F). Authigenic illite developed on crystal surfaces of cubic halite indicates the halite is a primary cement and predated illite precipitation. Comparable-shaped halite crystals were described as primary halite cements by Lowenstein and Hardie (1985) in the Saline Valley, California.

5.3. Carbonate cements

Carbonate cements are the most abundant diagenetic minerals in Es4x and range in abundance from 2.0% to 28.0% (Supplementary Material 1). Carbonate cements mainly consist of dolomite (2.0–25.0%, ave. 8.1%) and ankerite (2.0–10.0%, ave. 5.2%).

Dolomite cements occur as two phases: micritic and sparry dolomite. Micritic dolomite cement consists of dull, clay-sized crystals (Fig. 10A). Sparry dolomite (5–300 μm) typically occurs as intergranular, pore-filling cement and consists of rhombohedral and saddle-shaped crystals (Fig. 10B, C). Moreover, the saddle dolomite has sweeping extinction and curved crystal boundaries and typically is surrounded by solid bitumen (Fig. 10B). Micritic dolomite also occurs as a replacement of framework feldspar and, less commonly, lithic grains (Fig. 10A).

Ankerite occurs mainly as scattered euhedral rhombs (5–150 μm) and patchy aggregates (10–250 μm) (Figs. 7D, 10D and 10E). Dolomite cements are typically zoned and replaced by
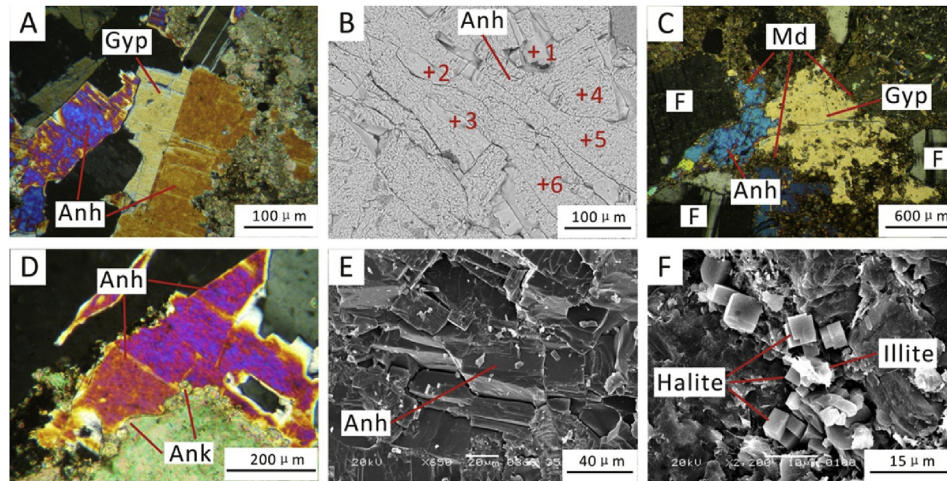
Fig. 7. Photomicrographs of evaporite cements in Es4x. (A) Gypsum enclosed and replaced by anhydrite laths, Well FS5, 4308.8 m; (B) BSE image showing anhydrite laths, Well F8, 4397.2 m; (C) Pore-filling gypsum and anhydrite and engulfed by micritic dolomite, Well F8, 4397.5 m; (D) Anhydrite engulfed by ankerite, Well FS5, 4484.8 m; (E) Anhydrite laths, Well F8, 3843.1 m; (F) Cubic halite crystals, Well FS3, 4867 m. Gyp = Gypsum, Anh = Anhydrite, Md = Micritic dolomite, Ank = Ankerite, F = Feldspar.
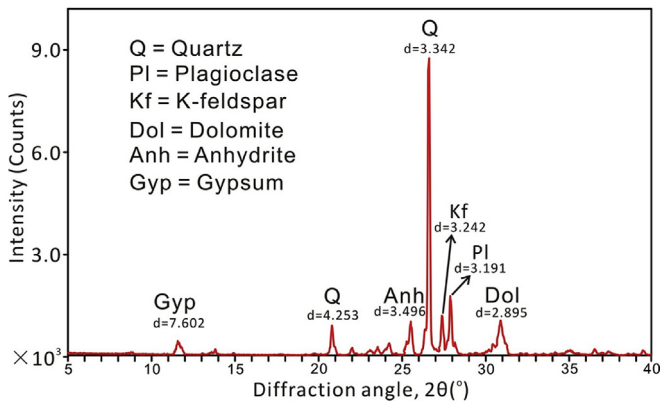
Fig. 8. X-ray diffraction pattern of sandstone sample from the Eocene Es4x interval at a depth of 4323 m. The XRD patterns show that quartz and feldspar are the most abundant minerals, followed in abundance by dolomite, anhydrite and then gypsum. d = diffraction peak.

ankerite (Fig. 10E). Ankerite cement commonly is enclosed by solid bitumen (Fig. 10D). Locally, ankerite fills grain fractures and feldspar dissolution pores (Fig. 10F). EDX confirms the identification of ankerite cements. In common with evaporite cements, dolomite and ankerite cements are most abundant in the depth range of 4300—4500 m (Fig. 9C, D).

5.4. Pyrite

Pyrite cements are either framboidal or nodular. Framboidal pyrite (<1.0%) is developed locally as spheroidal aggregates (2—50 μm in diameter) (Fig. 11A). Nodular pyrite (0.5—9.5%, ave. 3.1%; Supplementary Material 1) typically occurs as pore-filling cements (Fig. 11B) and as a replacement of framework grains as well as authigenic minerals (Fig. 11C, D). Most of the authigenic minerals are replaced by nodular pyrite including carbonate (Fig. 11C), gypsum and anhydrite cements (Fig. 11D). Nodular pyrite normally coexists with solid bitumen.
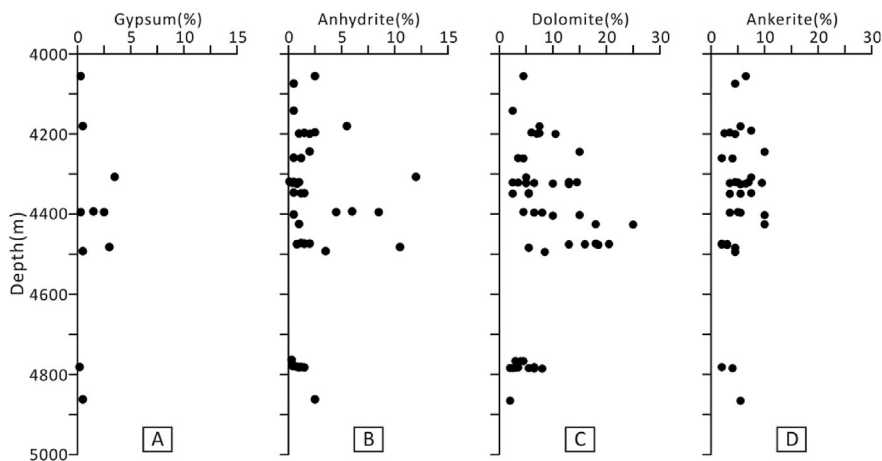
Fig. 9. (A) Plot showing variations in the percentage of gypsum cements with depth (10 data points from 4 boreholes); (B) Plot showing variations in the percentage of anhydrite cements with depth (46 data points from 7 boreholes); (C) Plot showing variations in the percentage of dolomite cements with depth (51 data points from 6 boreholes); (D) Plot showing variations in the percentage of ankerite cements with depth (35 data points from 7 boreholes). All data based on point counting.
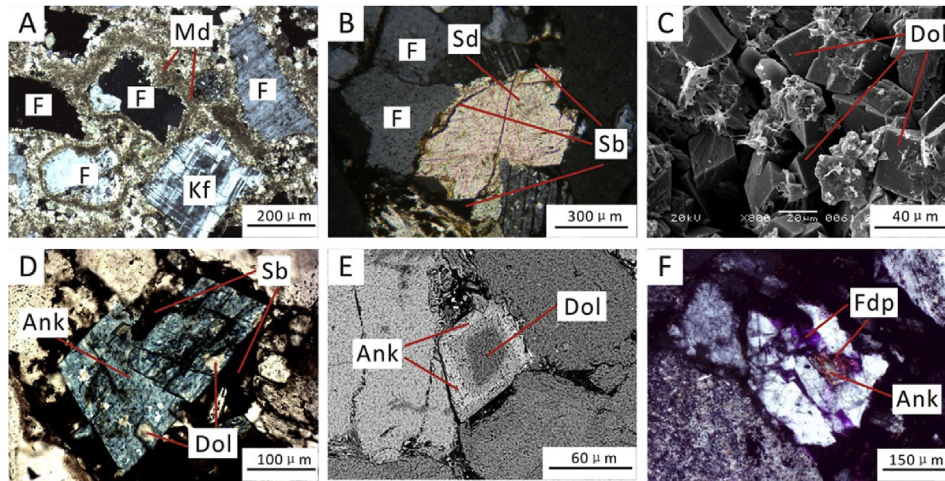
Fig. 10. Photomicrographs of carbonate cements and their spatial relationships in Es4x. (A) Micritic dolomite cement, Well FS4, 4476.2 m; (B) Saddle dolomite cement surrounded by solid bitumen, Well FS1, 4321.9 m; (C) Euhedral rhombic dolomite cement, Well FS10, 4323.7 m; (D) Rhombic ankerite cement surrounded by solid bitumen, Well FS1, 4321.9 m; (E) BSE image of a zoned dolomite and ankerite rhomb with increasing Fe content towards the rim of the crystal, Well FS1, 4321.9 m; (F) Feldspar dissolution pores filled with ankerite cements, Well FS3, 4785.7 m. Md = Micritic dolomite, Sd = Saddle dolomite, Dol = Dolomite, Ank = Ankerite, Sb = Solid bitumen, F = Feldspar, Kf = K-feldspar, Fdp = Feldspar dissolution pore.
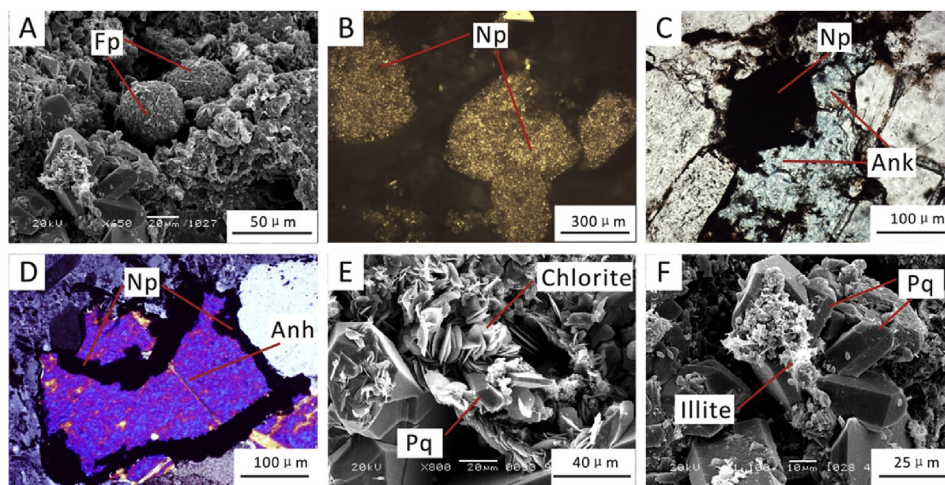
Fig. 11. Photomicrographs of pyrite, quartz and clay cements in Es4x. (A) SEM image showing framboidal pyrite, Well FS1, 4322.1 m; (B) Nodular pyrite under reflected light, Well FS4, 4476.2 m; (C) Ankerite replaced by nodular pyrite, Well FS3, 4867.0 m; (D) Anhydrite replaced by nodular pyrite, Well FS5, 4308.8 m; (E) SEM image showing pore-filling chlorite rosettes, Well FS3, 4867 m; (F) SEM image showing hair-like illite developed on the crystal surface of prismatic quartz. Fp = Framboidal pyrite, Np = Nodular pyrite, Ank = Ankerite, Anh = Anhydrite, Pq = Prismatic quartz.

5.5. Other authigenic minerals

Other minor authigenic minerals in Es4x include quartz cements and authigenic clays. Quartz cements (<1%) commonly occur as euhedral, prismatic crystals within intergranular pores (Fig. 11E, F). Authigenic clays are dominated by chlorite and illite that occur as pore-filling cements and as replacements of detrital feldspar. Authigenic chlorite occurs as small flakes and rosette crystals (Fig. 11E) whereas authigenic illite occurs as hair-like crystals and fibrous aggregates (Fig. 11F).

6. Porosity and permeability

Based on thin section observations complemented by SEM and BSE imaging, three types of porosity are recognized in Es4x: primary, secondary and micro-fracture porosity. According to point counting data, total porosity ranges from 0.1 to 3.5% with an average of 1.3% (Supplementary Material 1). Primary porosity (0.1–1.8%, ave. 0.7%) (Fig. 12A) consists of open intergranular pore spaces (Fig. 13A) and represents a significant percentage of the total porosity (15.0–100.0%, ave. 48.6%). Secondary porosity consists of intragranular and intergranular pores derived from dissolution of framework grains, and gypsum and anhydrite cements, respectively. Intragranular dissolution porosity (0.1–1.8%, ave. 0.6%) (Fig. 12B) is related to partial to extensive dissolution of detrital plagioclase as well as potassium feldspar. Dissolution of plagioclase and potassium feldspar is closely associated with the formation of authigenic clays and quartz cements (Fig. 13B). Gypsum (Fig. 13C) and anhydrite cements (Fig. 13D, E) are commonly dissolved and, locally, black solid bitumen fills cleavage planes and dissolution pores within anhydrite (Fig. 13F). Dissolution porosity of anhydrite (0.1–2.0%, ave. 0.7%) is higher than that of gypsum (0.1–0.5%, ave. 0.2%) (Fig. 12C, D). Micro-fractures commonly occur within anhydrite cements and range from 0.5 to 9 μm in width (Fig. 13G, H, I).
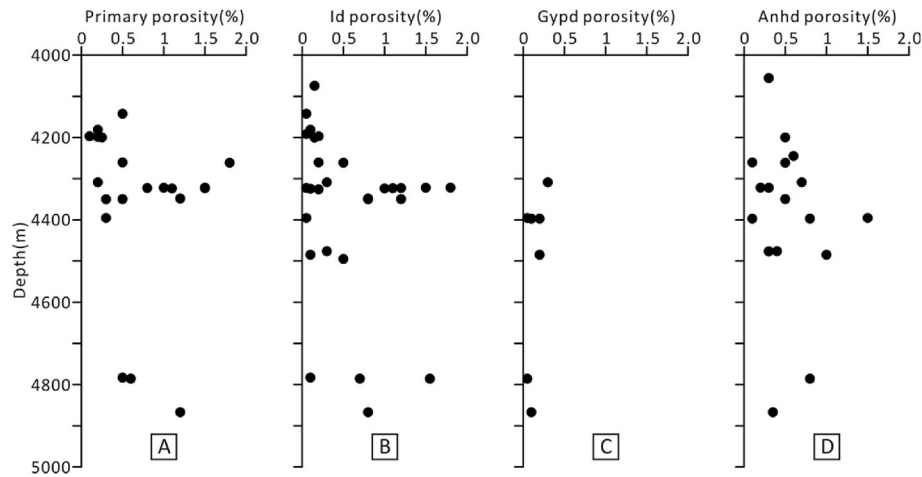
Fig. 12. Plots showing porosity types and variations with depth (Based on point counting of 53 thin sections from 7 boreholes in Es4x). Id = Intragranular dissolution, Gypd = Gypsum dissolution, Anhd = Anhydrite dissolution.
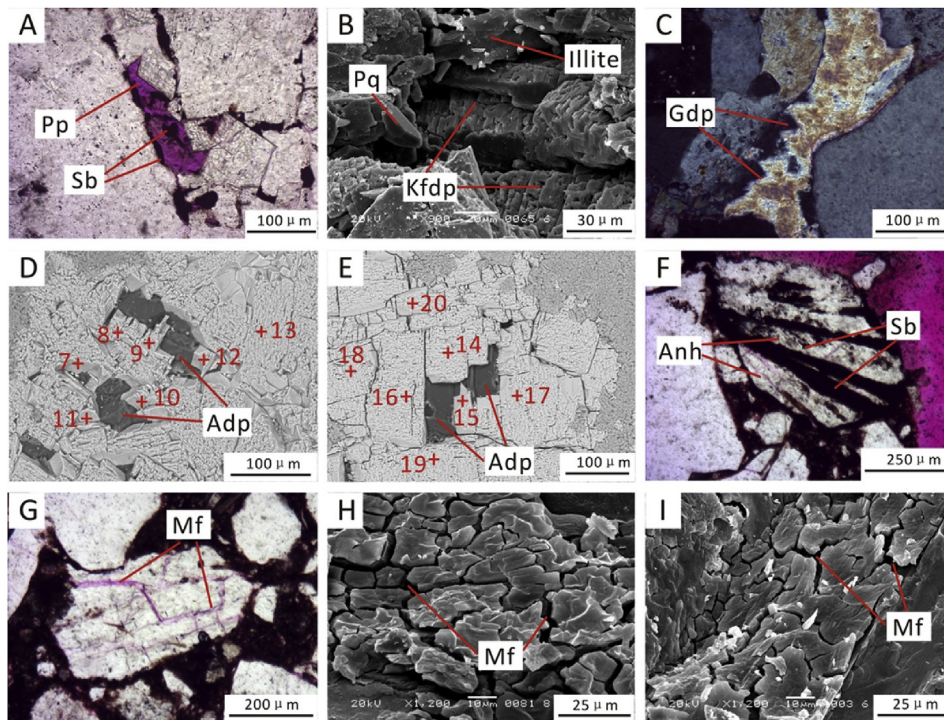
Fig. 13. (A) Primary pores, Well FS10, 4261.4 m; (B) Secondary porosity related to K-feldspar dissolution with by-products (authigenic quartz and illite), Well FS10. 4323.7 m; (C) Secondary porosity related to gypsum dissolution, Well FS5, 4308.8 m; (D) BSE image showing secondary porosity related to anhydrite dissolution, Well F8, 4397.2 m; (E) BSE image showing secondary porosity related to anhydrite dissolution, Well FS5, 4308.8 m; (F) Bitumen-filled cleavage planes and dissolution pores in anhydrite, Well F8, 4395.4 m; (G) Micro-fracture porosity within anhydrite cements, Well FS5, 4308.8 m; (H) Micro-fracture porosity within anhydrite cements, Well FS3, 4785.7 m; (I) Micro-fracture porosity within anhydrite cements, Well FS10, 4323.7 m. Pp = Primary pore, Sb = Solid bitumen, Kfdp = K-feldspar dissolution pore, Pq = Prismatic quartz, Gdp = Gypsum dissolution pore, Adp = Anhydrite dissolution pore, Anh = Anhydrite, Mf = Micro-fracture.

These fractures are irregular-shaped and relatively tortuous. Euhedral dolomite and ankerite crystals show little or no evidence of dissolution (Fig. 10C, E).

Reservoir characteristics are evaluated using porosity and permeability data determined for 73 plug samples from Es4x. A cross-plot of plug porosity and permeability for different lithofacies in Es4x show that porosities range from 2.8 to 10.7% (ave. 5.8%) for coarse-grained pebbly sandstones, 4.6—8.3% (ave. 6.1%) for medium- or coarse-grained sandstones, 0.4—5.6% (ave. 2.7%) for siltstone or fine-grained sandstones and finally, 0.9—5.0% (ave. 2.8%)

for matrix- and framework-supported conglomerates (Fig. 14). Permeabilities range from 0.262 to 12.100 mD (ave. 3.192 mD) for coarse-grained pebbly sandstones, 0.021 to 4.570 mD (ave. 1.288 mD) for medium- or coarse-grained sandstones, 0.005 to 1.260 mD (ave. 0.178 mD) for siltstone or fine-grained sandstones and finally, 0.007 to 1.830 mD (ave. 0.321 mD) for matrix- and framework-supported conglomerates (Fig. 14). In general, all lithofacies show wide variations in porosity and permeability and a relatively weak correlation between porosity and permeability (Fig. 14). The data indicate that coarse-grained pebbly sandstones and medium- to
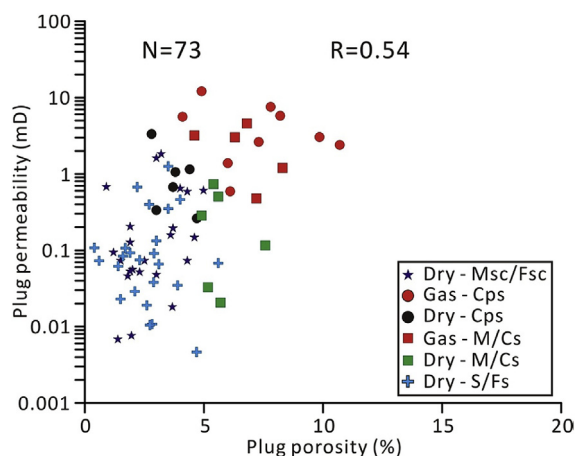
Fig. 14. Cross-plot of plug porosity and permeability for different lithofacies in Es4x (73 data points from 6 boreholes). Msc/Fsc = Matrix- or framework-supported conglomerate; Cps = Coarse-grained pebbly sandstone; M/Cs = Medium- or coarse-grained sandstone; S/Fs = Siltstone or fine sandstone.

coarse-grained sandstones of the middle-fan have the best reservoir properties and contain most hydrocarbons (Fig. 14). Inner-fan matrix- and framework-supported conglomerates and outer-fan siltstone or fine-grained sandstones have the lowest reservoir potential and contain no hydrocarbons (Fig. 14).

7. Mineral chemistry

7.1. Elemental mapping of anhydrite and carbonate cements

Backscatter electron (BSE) imaging and elemental mapping of calcium, magnesium, iron, potassium, aluminum, sulfur, silicon and carbon were undertaken on anhydrite- and carbonate-cemented samples in Es4x. Domains of relatively high contents of each element analyzed are shown in different colors on BSE images (Figs. 15 and 16).

Domains with bright tones for calcium and sulfur represent anhydrite cements (Fig. 15) whereas bright tones for calcium, magnesium and iron images represent ankerite cements (Fig. 16). Moreover, domains with bright tones on potassium, aluminum and

silicon define detrital feldspar and quartz grains (Figs. 15 and 16), and bright tones on carbon represent solid bitumen (Fig. 16).

Chemical compositions of anhydrite and carbonate cements were determined by quantitative SEM-EDS point analysis. In total, 20 data points were obtained on anhydrite cements (Figs. 7B, 13D and 13E). Elemental weight percentages (%) for Ca, S, and O were used to calculate moles and were normalized to molecular percentages (Table 1). The data show that anhydrite cements are very pure with high concentrations of O (48.5–80.0 mol %, ave. 68.9 mol %) and relatively low concentrations of Ca (10.8–24.9 mol %, ave. 16.0 mol %) and S (9.1–28.3 mol %, ave. 15.2 mol %).

Thirty six (36) points were analyzed from zoned carbonate cements. Elemental weight percentages (%) for Mg, Ca and Fe were used to calculate moles and were normalized to molecular percentages (Table 2). These percentages were plotted on a ternary diagram with calcite, magnesite and siderite end members (Fig. 17). The results define two distinct clusters (Fig. 17). Dolomite cements contain very low concentrations of $FeCO_3$ (up to 3.5 mol %, ave. 1.3 mol %) but significant contents of $MgCO_3$ (38.0–49.4 mol %, ave. 45.0 mol %). Ankerite cements are enriched in $FeCO_3$ (11.3–21.5 mol %, ave. 15.7 mol %) and $MgCO_3$ (17.0–41.0 mol %, ave. 27.9 mol %).

7.2. Stable isotopes

Eleven (11) $\delta^{13}C$ and $\delta^{18}O$ isotope measurements on micritic dolomite and ankerite cements in Es4x are plotted in X-Y space (Fig. 18). Micritic dolomite cements have a range of $\delta^{18}O$ values from −11.60 to −9.50‰ and $\delta^{13}C$ values from −7.45 to −2.57‰. Ankerite cements have more negative $\delta^{18}O$ values from −17.85 to −11.82‰ and similar $\delta^{13}C$ values from −7.12 to −3.70‰ (Table 3).

Seven (7) anhydrite-cemented samples show anomalous enrichment in $\delta^{34}S$ (+21.2 to +37.8‰, ave. +33.5‰, Table 4). $\delta^{34}S$ values for seven pyrite-cemented samples define two populations corresponding with framboidal pyrite (−3.9 to +5.7‰, Table 4) and nodular pyrite (+17.1 to +37.0‰, Table 4).

7.3. Fluid inclusions

Microthermometric measurements were conducted on fluid inclusions within pore-filling and fracture-filling anhydrite cements in Es4x (Fig. 19A, B). Most aqueous inclusions trapped within anhydrite cements contain measurable, two-phase inclusions
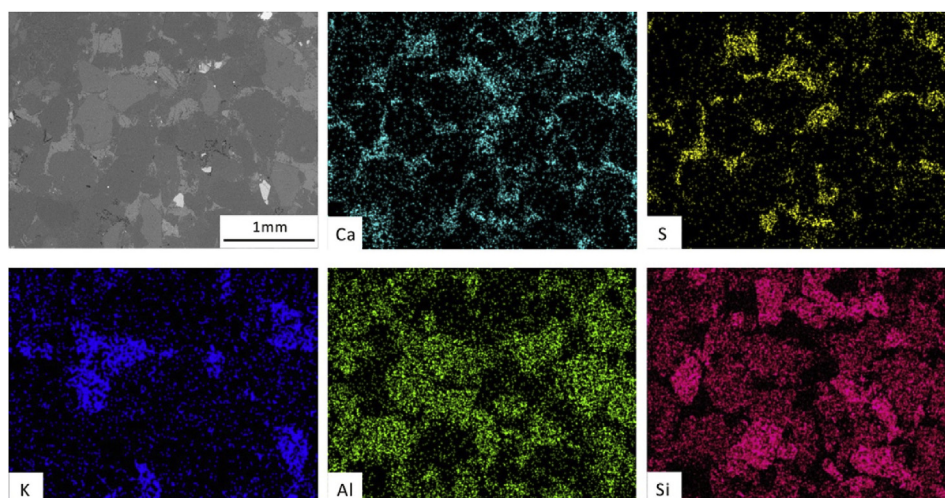
Fig. 15. Backscattered electron images (BSE) of anhydrite cements with elemental maps Ca, S, K, Al and Si in Well F8, 4397.2 m.
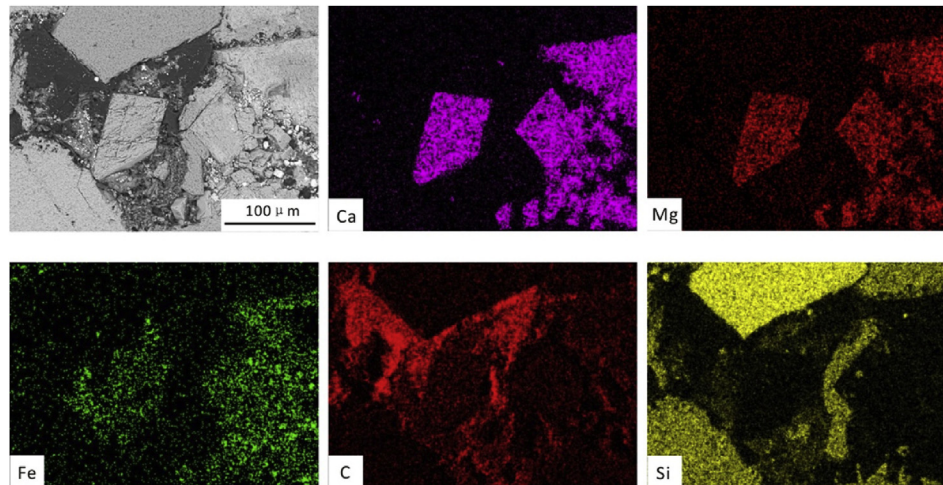
Fig. 16. Backscattered electron images (BSE) of carbonate cements with elemental maps Ca, Mg, Fe, C and Si in Well FS1, 4321.9 m.

Table 1
EDX analyses of anhydrite cements in Es4x.

Well	Depth (m)	Strata	Number	Molecular (%)		
				O	S	Ca
F8	4397.15	Es4x	1	51.9	23.2	24.9
F8	4397.15	Es4x	2	73.6	12.8	13.6
F8	4397.15	Es4x	3	77.9	9.9	12.2
F8	4397.15	Es4x	4	73.5	12.2	14.3
F8	4397.15	Es4x	5	72.4	12.4	15.2
F8	4397.15	Es4x	6	68.3	15.4	16.3
F8	4397.15	Es4x	7	48.5	28.3	23.2
F8	4397.15	Es4x	8	67.9	14.7	17.4
F8	4397.15	Es4x	9	66.0	16.3	17.7
F8	4397.15	Es4x	10	67.3	15.7	17.0
F8	4397.15	Es4x	11	70.3	13.8	15.8
F8	4397.15	Es4x	12	74.2	12.0	13.8
F8	4397.15	Es4x	13	62.3	18.8	18.9
FS5	4308.8	Es4x	14	73.0	13.5	13.5
FS5	4308.8	Es4x	15	71.8	13.7	14.5
FS5	4308.8	Es4x	16	75.8	12.0	12.3
FS5	4308.8	Es4x	17	72.6	13.4	14.0
FS5	4308.8	Es4x	18	80.0	9.1	10.8
FS5	4308.8	Es4x	19	60.9	20.6	18.4
FS5	4308.8	Es4x	20	69.0	15.6	15.4

Table 2
EDX analyses of carbonate cements in Es4x.

Well	Depth (m)	Strata	Carbonate cements	Molecular (%)		
				CaCO$_3$	MgCO$_3$	FeCO$_3$
FS1	4321.9	Es4x	Dolomite	54.4	45.6	0.0
FS1	4321.9	Es4x	Dolomite	53.8	46.2	0.0
FS1	4321.9	Es4x	Dolomite	54.2	45.8	0.0
FS1	4321.9	Es4x	Dolomite	53.5	46.5	0.0
FS1	4321.9	Es4x	Dolomite	54.1	45.9	0.0
FS1	4321.9	Es4x	Dolomite	55.0	45.0	0.0
FS5	4308.8	Es4x	Dolomite	62.0	38.0	0.0
FS5	4308.8	Es4x	Dolomite	55.3	43.1	1.7
FS5	4308.8	Es4x	Dolomite	53.8	44.4	1.8
FS5	4308.8	Es4x	Dolomite	54.8	43.4	1.8
FS5	4308.8	Es4x	Dolomite	51.7	46.1	2.2
FS5	4308.8	Es4x	Dolomite	55.1	42.4	2.5
FS5	4308.8	Es4x	Dolomite	51.9	45.6	2.5
FS5	4308.8	Es4x	Dolomite	49.4	48.1	2.5
FS5	4308.8	Es4x	Dolomite	47.7	49.4	3.0
FS5	4308.8	Es4x	Dolomite	51.4	45.1	3.5
FS1	4321.9	Es4x	Ankerite	50.9	35.9	13.2
FS1	4321.9	Es4x	Ankerite	55.8	26.8	17.5
FS1	4321.9	Es4x	Ankerite	54.6	32.4	13.0
FS1	4321.9	Es4x	Ankerite	57.1	25.2	17.7
FS1	4321.9	Es4x	Ankerite	53.0	32.6	14.4
FS1	4321.9	Es4x	Ankerite	53.5	31.2	15.3
FS1	4321.9	Es4x	Ankerite	58.1	22.5	19.4
FS1	4321.9	Es4x	Ankerite	65.3	17.0	17.7
FS1	4321.9	Es4x	Ankerite	57.8	30.7	11.5
FS5	4308.8	Es4x	Ankerite	47.7	41.0	11.3
FS5	4308.8	Es4x	Ankerite	49.4	39.2	11.4
FS5	4308.8	Es4x	Ankerite	51.5	36.1	12.4
FS5	4308.8	Es4x	Ankerite	53.6	28.9	17.5
FS5	4308.8	Es4x	Ankerite	59.8	21.0	19.3
FS5	4308.8	Es4x	Ankerite	58.5	20.0	21.5
FS5	4308.8	Es4x	Ankerite	62.3	17.1	20.5
FS5	4308.8	Es4x	Ankerite	60.8	22.7	16.6
FS5	4308.8	Es4x	Ankerite	64.6	21.1	14.3
FS5	4308.8	Es4x	Ankerite	57.7	26.8	15.6
FS5	4308.8	Es4x	Ankerite	56.6	29.6	13.8

≥5 μm in size that have small vapor bubbles at room temperatures (Fig. 19A, B). Other aqueous inclusions observed within anhydrite cements are too small to be measured. Homogenization temperatures (Ths) were obtained from 65 aqueous inclusions and ice final melting temperatures (Tms) were determined for 33 of the 65 inclusions (Table 5). The same preferential orientation and relatively uniform elongate shape of fluid inclusions in most of FIAs suggest that the FIAs are primary and were trapped at the same time during crystal growth of anhydrite (Fig. 19A, B). In addition, most of FIAs are characterized by consistent Th values within a FIA (temperature differences commonly less than 10 °C) and indicate the FIAs probably have not been altered by thermal reequilibration after their entrapment (e.g. Goldstein, 2001).

Th values for aqueous inclusions range from 100.5 to 145.2 °C with a peak at 120—130 °C (Fig. 20A). The calculated salinities for aqueous inclusions ranges from 14.2 to 21.9 wt % NaCl equivalent with a peak at 16—18 wt % NaCl equivalent (Fig. 20B). No notable differences of Th and salinity occur between pore-filling and fracture-filling anhydrite cements.

8. Discussion

8.1. Origin and transformation of evaporite cements

As described above, early burial fluids were characterized by high salinity associated with arid climatic conditions that favored precipitation of gypsum and subordinate halite. Replacement of
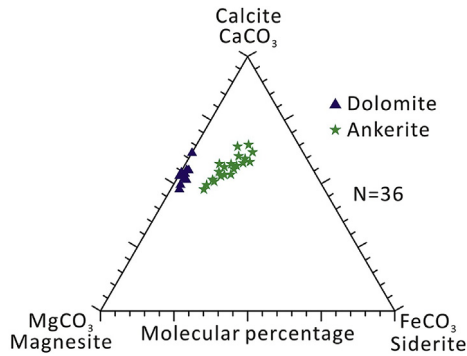
Fig. 17. Chemical compositions of carbonate cements (36 data points from 2 boreholes in Es4x).

Fig. 18. Cross-plot of carbon and oxygen isotopic compositions of micritic dolomite and ankerite cements (11 data points from 6 boreholes in Es4x).

concluded that anhydrite is a dehydration product of gypsum. Large-scale dehydration of gypsum results in 38% by volume of water release (Bjorlykke, 1993; Jowett et al., 1993). Therefore, the crystal structure of anhydrite (precursor gypsum) was disrupted by the loss of structural water (e.g. Warren, 2006; Harrison, 2012) which resulted in the development of tortuous dehydration fractures within anhydrite cements (Fig. 13G, H, I). Importantly, the released fluids were hypersaline as evidenced by 14.2–21.9 wt % NaCl equivalent of aqueous inclusions within anhydrite cements.

8.2. Origin of associated diagenetic minerals (carbonate and pyrite cements)

Lacustrine sedimentary dolomites in the Eocene Es4 interval have $\delta^{18}O_{PDB}$ values ranging from −1.50 to +0.33‰ (ave. −0.85‰) (Liu, 1998). Assuming a water temperature of 10 °C, the $\delta^{18}O_{SMOW}$ value of lake water can be calculated as −5.4‰ based on oxygen isotopic equilibrium fractionation between dolomite and water (see Irwin et al., 1977). This value is assumed to represent the oxygen isotopic composition of pore waters from which early dolomite cements were precipitated. Calculated precipitation temperatures ranged from 57.5 to 72.8 °C for micritic dolomite cements (Table 3; Irwin et al., 1977) and indicate that micritic dolomite cements are typical eogenetic products formed at temperatures less than 70 °C (cf. Morad et al., 2000).

Micritic dolomite cements in Es4x have negative $\delta^{13}C$ values ranging from −7.45 to −2.57‰. Based on the presence of organic matter in adjacent mudstones (TOC contents up to 18.6%, Guo et al., 2010) and diffusive supply of sulfate from depositional water (cf. Irwin et al., 1977; Curtis, 1978), it is likely that microbial sulfate reduction (MSR) and other microbial respiratory pathways provided ^{12}C-enriched carbon that would have gone to form the micritic dolomite cements at relatively low temperatures (57.5–72.8 °C). This conclusion is consistent with a maximum temperature range (60–80 °C) over which MSR is known to occur (Machel, 2001). Low $\delta^{13}C$ values in carbonate cements formed at relatively low temperatures have been linked to MSR as in the Coorong Region, Early Holocene, South Australia (Wright, 1999) and in the Hellín Basin, Late Miocene, SE Spain (Lindtke et al., 2011).

Table 3
Oxygen and carbon isotopic compositions, calculated precipitation temperatures of carbonate cements in Es4x.

Well	Depth (m)	Strata	Carbonate cements	$\delta^{13}C$ (‰PDB)	$\delta^{18}O$ (‰PDB)	$\delta^{18}O_{water}$ (‰SMOW)	T-precip. (°C)
F8	4397.15	Es4x	Micritic dolomite	−2.57	−9.50	−5.4	57.5
FS5	4308.8	Es4x	Micritic dolomite	−5.19	−9.71	−5.4	59.0
FS5	4308.8	Es4x	Micritic dolomite	−5.45	−11.60	−5.4	72.8
FS4	4476.15	Es4x	Micritic dolomite	−7.45	−10.89	−5.4	67.5
FS10	4321.3	Es4x	Ankerite	−6.82	−13.20	0	134.8
FS10	4320.9	Es4x	Ankerite	−6.38	−15.18	0	155.3
FS5	4304.9	Es4x	Ankerite	−5.33	−12.31	0	126.0
FS3	4867	Es4x	Ankerite	−7.12	−17.85	0	185.1
FS3	4867	Es4x	Ankerite	−6.85	−17.83	0	185.0
F8	4198.91	Es4x	Ankerite	−3.70	−11.82	0	121.3
FS1	4322.1	Es4x	Ankerite	−6.76	−17.79	0	184.4

gypsum by anhydrite is recorded by gypsum pseudomorphs preserved in anhydrite laths (Fig. 7A) and indicates progressive dehydration of primary gypsum (cf. Amadi et al., 2012). Precipitation of anhydrite cements probably occurred at 100.5–145.2 °C as evidenced by homogenization temperatures of aqueous inclusions within these cements (Fig. 20A). Such temperatures also are consistent with complete conversion of gypsum to anhydrite that is considered to occur over a temperature range of 100–150 °C (Jordan and Astilleros, 2006; Harrison, 2012). Therefore, it is

Moreover, gypsum is engulfed or replaced by micritic dolomite cement (Fig. 7C) and resembles replacement of calcium sulfates by dolomite cements related to MSR as observed elsewhere (e.g. Muchez et al., 2008). Importantly, burial fluids are reduced under these conditions (Curtis, 1978) and, thus, MSR resulted in the formation of framboidal pyrite aggregates (Fig. 11A; cf. Bottrell et al., 2000; Morad et al., 2000). $\delta^{34}S$ fractionation between framboidal pyrite (−3.9 to +5.7‰) and precursor anhydrite (+21.2 to +37.8‰) is comparable to positive $\delta^{34}S$ values in sulfate and negative $\delta^{34}S$

Table 4
Sulfur isotopic compositions of anhydrite and pyrite cements in Es4x.

Well	Depth (m)	Strata	$\delta^{34}S_{Anhydrite}$ (‰CDT)	$\delta^{34}S_{Pyrite}$ (‰CDT)	Pyrite occurrence
F8	3843.1	Es4x	35.7	Nd	
F8	4199.41	Es4x	Nd	17.7	Nodular
F8	4199.91	Es4x	35.3	2.7	Framboidal
F8	4397.15	Es4x	35.6	17.1	Nodular
FS10	4323.7	Es4x	36.2	37.0	Nodular
FS3	4867	Es4x	37.8	5.7	Framboidal
FS4	4476.15	Es4x	21.2	−3.9	Framboidal
FS5	4308.8	Es4x	32.8	21.5	Nodular

Nd = No data.
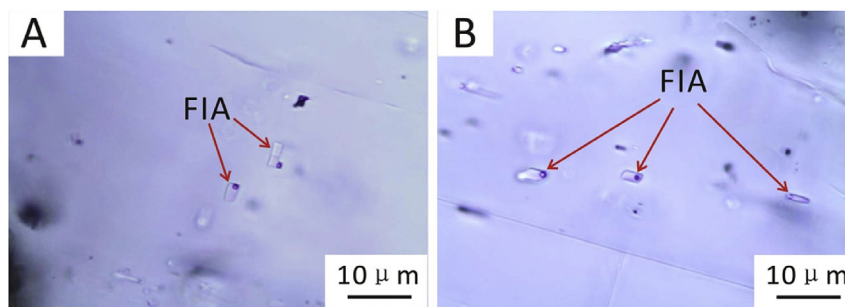
Fig. 19. Photomicrographs of aqueous inclusions in anhydrite cements. (A) Pore-filling anhydrite. (B) Fracture-filling anhydrite. AI = Aqueous inclusion.

values in sulfide (e.g. pyrite) produced by MSR in lacustrine sequences as reported by Cai et al. (2005), Alonso-Azcárate et al. (2006) and Lindtke et al. (2011).

Ankerite cements were precipitated after feldspar dissolution in Es4x as evidenced by feldspar dissolution pores filled with ankerite cements (Fig. 10F). Previous studies have shown that pore waters become isotopically heavier in $\delta^{18}O$ with increasing temperature as the isotopic compositions are modified by feldspar dissolution (Fayek et al., 2001), as well as, other fluid-rock interactions (e.g. transformation of smectitic clay minerals in adjacent shales) (e.g. Fisher and Boles, 1990; Anjos et al., 2000). Other workers (e.g. Kantorowicz, 1985; Anjos et al., 2000; Yuan et al., 2015) have estimated that $\delta^{18}O_{SMOW}$ values of deep-burial pore-fluids from which ferran carbonate cements precipitated ranged from −3 to +2‰. In the present study, an average $\delta^{18}O_{SMOW}$ value of 0.0‰ was assumed for the fluids from which ankerite cements were precipitated. Based on this assumption, precipitation temperatures of ankerite can be calculated as 121.3−185.1 °C for ankerite (Table 3, Irwin et al., 1977) indicating that ankerite cements are mesogenetic products precipitated at temperatures exceeding 70 °C (cf. Morad et al., 2000).

Dissolved gypsum and anhydrite cements (Fig. 13C, D, E) and black solid bitumen filling cleavage planes and dissolution pores within anhydrite (Figs. 5E and 13F) probably indicate that thermochemical sulfate reduction (TSR) occurred at elevated temperatures (cf. Machel, 2001). Saddle dolomite cements are interpreted to be precipitated from hypersaline brines at relatively high temperatures (e.g. Warren, 2000; Huang et al., 2014) and probably are by-products of TSR as evidenced by saddle dolomite surrounded by solid bitumen (Fig. 10B; e.g. Warren, 2000; Vandeginste et al., 2009). Ankerite cements that replace anhydrite cements (Fig. 7D) are enclosed by solid bitumen (Figs. 10D and 16) in Es4x demonstrating that ankerite cements could have been derived as by-products of TSR as reflected in the negative $\delta^{13}C$ values (−7.12 to −3.70‰) and high calculated temperatures (121.3−185.1 °C). Precipitation temperatures of ankerite cements also are consistent with a temperature range for TSR of 100−140 °C and, rarely,

160−180 °C (cf. Machel, 2001). Moreover, the scatter in $\delta^{13}C$ values for replacive ankerite (Fig. 18) indicates that, at the initial stage of TSR, pore-fluids were dominated by bicarbonate species that resulted from the dissolution of early-formed dolomite. As TSR continued, more organic carbon was incorporated into ankerite resulting in lighter carbon isotope values (Fig. 18; cf. Worden et al., 2000). Similar positive correlations between the carbon and oxygen isotope values of carbonate cements derived from TSR have been reported elsewhere (Worden et al., 2000; Vandeginste et al., 2009). Importantly, sources of Mg^{2+} and Fe^{2+} for ankerite formation were probably derived from clay-mineral transformations (smectite to illite) in adjoining mudstones which likely were undergoing hydrocarbon maturation (cf. Hendry et al., 2000).

Nodular pyrite probably was a by-product of TSR as evidenced by anhydrite as well as ankerite engulfed by nodular pyrite (Fig. 11C, D; cf. Morad et al., 2000; Machel, 2001; Hao et al., 2015). Nodular pyrite has comparable $\delta^{34}S$ values (+17.1 to +37.0‰) to precursor anhydrite (+21.2 to +37.8‰). Thus, no significant sulfur isotope fractionation took place between parent sulfate and reduced products and indicates a relatively closed system during TSR (cf. Machel, 2001; Cai et al., 2005; Hao et al., 2015).

8.3. Reservoir characteristics

Evaporite evolution in response to progressive burial had a critical influence on sublacustrine fan reservoir quality. MSR processes are inferred to have dominated at shallow burial depths and resulted in formation of abundant micritic dolomite (Fig. 10A) and subordinate framboidal pyrite cements (Fig. 11A). These authigenic cements pervasively filled primary pores and resulted in deterioration of reservoir quality (Fig. 21). Dehydration fractures within anhydrite cements probably enhanced reservoir quality and increased reservoir permeability by connecting isolated pores. Evidence for this inference is based on some lithofacies displaying low porosity but relatively high permeability (Fig. 14).

Evaporites probably reacted with hydrocarbons via thermochemical sulfate reduction (TSR) at elevated temperatures under

Table 5
Microthermometric data of aqueous fluid inclusions within anhydrite cements in Es4x.

Well	Depth (m)	Occurrence	Th (°C)	Tm (°C)	Salinity (wt.%NaCl)	FIA
F8	3843.1	Fracture-filling	121.3	15	18.6	1
F8	3843.1	Fracture-filling	125.1	10.3	14.2	1
F8	3843.1	Fracture-filling	125.5	13.7	17.5	1
F8	3843.1	Fracture-filling	118.6	Undetectable	Undetectable	2
F8	3843.1	Fracture-filling	125.5	16.3	19.7	2
F8	3843.1	Fracture-filling	123.2	11.3	15.3	2
F8	3843.1	Fracture-filling	128.5	14	17.8	2
F8	3843.1	Fracture-filling	132.2	14.5	18.2	3
F8	3843.1	Fracture-filling	135.6	17.8	20.8	3
F8	3843.1	Fracture-filling	138.6	18.7	21.5	4
F8	3843.1	Fracture-filling	131.2	16.5	19.8	4
F8	3843.1	Fracture-filling	112.5	Undetectable	Undetectable	5
F8	3843.1	Fracture-filling	118.7	Undetectable	Undetectable	5
F8	4199.51	Pore-filling	100.5	Undetectable	Undetectable	1
F8	4199.51	Pore-filling	107.5	Undetectable	Undetectable	1
F8	4199.51	Pore-filling	110.2	11.5	15.5	2
F8	4199.51	Pore-filling	109.5	10.5	14.5	2
F8	4199.51	Pore-filling	112.3	Undetectable	Undetectable	2
F8	4397.15	Fracture-filling	130.6	Undetectable	Undetectable	1
F8	4397.15	Fracture-filling	135.3	Undetectable	Undetectable	1
F8	4397.15	Fracture-filling	127.6	12.4	16.3	1
F8	4397.15	Fracture-filling	131.2	12.9	16.8	1
F8	4397.15	Fracture-filling	133.5	Undetectable	Undetectable	1
F8	4397.15	Fracture-filling	142.5	14.5	18.2	2
F8	4397.15	Fracture-filling	141.5	16.6	19.9	2
F8	4397.15	Fracture-filling	145.2	18.5	21.3	2
FS5	4308.8	Pore-filling	118.2	Undetectable	Undetectable	1
FS5	4308.8	Pore-filling	120.5	11.5	15.5	1
FS5	4308.8	Pore-filling	119.8	Undetectable	Undetectable	1
FS5	4308.8	Pore-filling	120.3	Undetectable	Undetectable	1
FS5	4308.8	Pore-filling	125.3	12.3	16.2	2
FS5	4308.8	Pore-filling	127.2	11.8	15.8	2
FS5	4308.8	Pore-filling	128.5	13.3	17.2	2
FS5	4308.8	Pore-filling	130.2	12.9	16.8	3
FS5	4308.8	Pore-filling	135.6	12.2	16.1	3
FS5	4308.8	Pore-filling	115.3	Undetectable	Undetectable	4
FS5	4308.8	Pore-filling	118.2	Undetectable	Undetectable	4
FS5	4308.8	Pore-filling	120.5	Undetectable	Undetectable	4
FS5	4308.8	Pore-filling	119.5	Undetectable	Undetectable	4
FS5	4308.8	Pore-filling	123.4	Undetectable	Undetectable	5
FS5	4308.8	Pore-filling	125.2	Undetectable	Undetectable	5
FS5	4308.8	Pore-filling	125.2	Undetectable	Undetectable	5
FS5	4308.8	Pore-filling	120.3	Undetectable	Undetectable	5
FS5	4305.2	Pore-filling	132.5	15.7	19.2	1
FS5	4305.2	Pore-filling	130.8	13	16.9	1
FS5	4305.2	Pore-filling	135.2	14.4	18.1	2
FS5	4305.2	Pore-filling	138.6	17.4	20.5	2
FS5	4305.2	Pore-filling	139.2	19.3	21.9	2
FS5	4305.2	Pore-filling	125.7	Undetectable	Undetectable	3
FS5	4305.2	Pore-filling	126.8	Undetectable	Undetectable	3
FS5	4305.2	Pore-filling	129.5	Undetectable	Undetectable	3
FS5	4305.2	Pore-filling	128.2	13.6	17.4	3
FS5	4305.2	Pore-filling	125.6	12.6	16.5	3
FS5	4305.2	Pore-filling	120.3	Undetectable	Undetectable	4
FS5	4305.2	Pore-filling	117.5	Undetectable	Undetectable	4
FS5	4305.2	Pore-filling	121.2	Undetectable	Undetectable	4
FS5	4305.2	Pore-filling	122.5	13.3	17.2	4
FS5	4305.2	Pore-filling	105.2	Undetectable	Undetectable	5
FS5	4305.2	Pore-filling	108.5	Undetectable	Undetectable	5
FS5	4305.2	Pore-filling	112.5	Undetectable	Undetectable	5
FS5	4305.2	Pore-filling	110.2	Undetectable	Undetectable	5
FS5	4305.2	Pore-filling	115.6	Undetectable	Undetectable	6
FS5	4305.2	Pore-filling	116.5	Undetectable	Undetectable	6
FS5	4305.2	Pore-filling	115.6	12.4	16.3	6
FS5	4305.2	Pore-filling	118.2	12.6	16.5	6

relatively deep burial conditions and resulted in dissolution of gypsum and anhydrite cements. Dissolution of gypsum and anhydrite (Fig. 13C, D, E), related to TSR, generated saddle dolomite, ankerite and nodular pyrite cements as by-products that precipitated in and occluded adjacent pores (Fig. 21; cf. Hao et al., 2015). Importantly, no significant sulfur isotope fractionation occurred

between parent sulfate and reduced products. Thus, it can be concluded that the rock-water interactions occurred in a relatively closed system and that few dissolution products were transported out of the system (cf. Machel, 2001; Bjørlykke and Jahren, 2012). Therefore, TSR contributed little to the net porosity of the reservoirs. Feldspar dissolution and resultant precipitation of by-
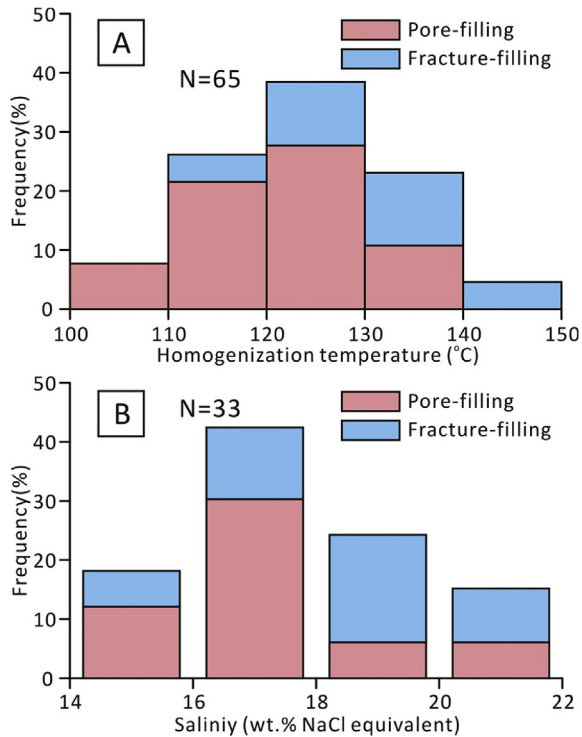
Fig. 20. (A) Histograms of homogenization temperatures (Th) of aqueous inclusions in anhydrite cements in Es4x (65 data points from 2 boreholes). (B) Histograms of calculated salinity of aqueous inclusions in anhydrite cements in Es4x (33 data points from 2 boreholes).
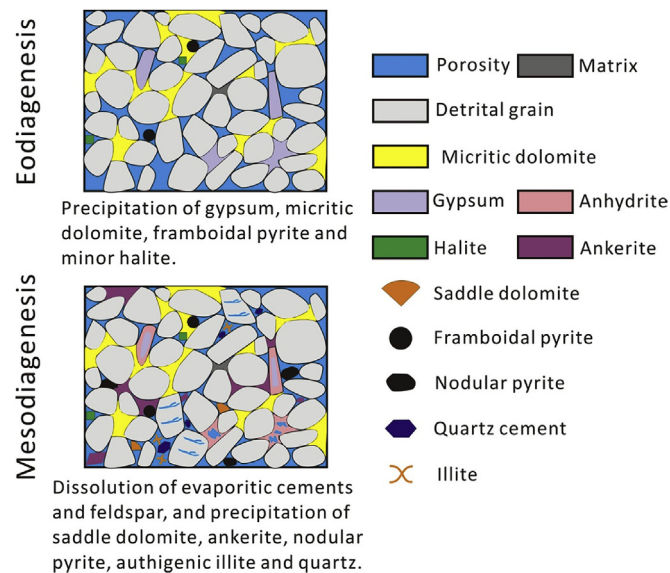
Fig. 21. Schematic diagram showing typical diagenetic products formed during eodiagenesis and mesodiagenesis.

products (e.g. authigenic quartz, illite) in adjacent pores indicates a relatively closed system (Fig. 21; cf. Chuhan et al., 2001; Bjørlykke and Jahren, 2012). Therefore, net porosities created by feldspar dissolution are not high (cf. Giles and de Boer, 1990) and are probably less than 0.25% (Yuan et al., 2015).

Coarse-grained pebbly sandstones and medium- to coarse-grained sandstones of the middle-fan are characterized by better sorting and lower matrix content compared to inner-fan matrix-

and framework-supported conglomerates and outer-fan siltstone and fine-grained sandstones. As a consequence, middle-fan lithofacies contain significant primary porosity (Fig. 13A) and more hydrocarbons than inner-fan and outer-fan lithofacies (Fig. 14).

9. Conclusions

This study on burial evolution of evaporites in sublacustrine fan reservoirs of Eocene Es4x, Dongying Depression, Bohai Bay Basin, China, has revealed that evaporite and related diagenetic processes critically influenced reservoir quality. Two units of evaporites, located at the bottom and the top of Es4x in cumulative thicknesses of more than 1600 m are predominantly in the form of anhydrite with subordinate gypsum. Microbial sulfate reduction (MSR) probably occurred at shallow burial conditions and favored precipitation of micritic dolomite and framboidal pyrite which resulted in deterioration of reservoir quality. During anhydritization of gypsum, large volumes of water were released and resulted in the formation of dehydration fractures within anhydrite cements. Dissolution of gypsum and anhydrite related to thermochemical sulfate reduction (TSR) at elevated temperatures under relatively deep burial conditions generated saddle dolomite, ankerite and nodular pyrite cements as by-products that precipitated in and occluded adjacent pores. A lack of significant sulfur isotope fractionation between parent sulfate and reduced products indicates TSR occurred in a relatively closed system and that few dissolution products were transported out of the system. Therefore, TSR contributed little to the net porosity of the reservoirs. Dissolution of feldspar probably occurred in a relatively closed system and contributed little to reservoir quality. High-quality reservoirs in Es4x are middle-fan lithofacies with better sorting, porosity, permeability and more hydrocarbons than inner- and outer-fan lithofacies. Sublacustrine-fan, rift deposits with associated evaporites are widely developed in eastern China and worldwide and, therefore, the results of this study have wide application to lacustrine reservoirs of similar tectono-sedimentary and diagenetic origin. The recognition of dehydration fractures in anhydrite cement that enhanced reservoir quality and increased reservoir permeability by connecting isolated pores represents a new contribution to the field of sandstone diagenesis.

Appendix A. Supplementary data

Supplementary data related to this article can be found at http://dx.doi.org/10.1016/j.marpetgeo.2016.05.014.

References

Alonso-Azcárate, J., Bottrell, S.H., Mas, J.R., 2006. Synsedimentary versus metamorphic control of S, O and Sr isotopic compositions in gypsum evaporites from the Cameros Basin. Spain. Chem. Geol. 234, 46—57.

Amadi, F.Q., Major, B.P., Baria, L.R., 2012. Origins of gypsum in deep carbonate reservoirs: implications for hydrocarbon exploration and production. AAPG Bull. 96, 375—390.

Anjos, S.M.C., De Ros, L.F., De Souza, R.S., De Assis Silva, C.M., Sombra, C.L., 2000. Depositional and diagenetic controls on the reservoir quality of lower cretaceous Pendência sandstones, Potiguar rift basin. Braz. AAPG Bull. 84, 1719–1742.

Bahadori, A., Carranza, E.J.M., Soleimani, B., 2011. Geochemical analysis of evaporite sedimentation in the gachsaran formation, Zeloi oil field, southwest Iran. J. Geochem. Explor. 111, 97–112.

Baruah, M.K., Gogoi, P.C., Kotoky, P., 2000. Sulphate behaviour from dissolution of gypsum in organic acids. Fuel 79, 211–216.

Bildstein, O., Worden, R.H., Brosse, E., 2001. Assessment of anhydrite dissolution as the rate-limiting step during thermochemical sulfate reduction. Chem. Geol. 176, 173–189.

Bjørlykke, K., 1993. Fluid flow in sedimentary basins. Sediment. Geol. 86, 137–158.

Bjørlykke, K., Jahren, J., 2012. Open or closed geochemical systems during diagenesis in sedimentary basins: constraints on mass transfer during diagenesis and the prediction of porosity in sandstone and carbonate reservoirs. AAPG Bull. 96, 2193–2214.

Bodnar, R.J., 1993. Revised equation and table for determining the freezing point depression of H_2O-NaCl solutions. Geochim. Cosmochim. Acta 57, 683–684.

Bottrell, S.H., Parkes, R.J., Cragg, B.A., Raiswell, R., 2000. Isotopic evidence for deep anoxic pyrite oxidation and stimulation of bacterial sulphate reduction. J. Geol. Soc. Lond. 157, 711–714.

Cai, C., Worden, R.H., Wolff, G.A., Bottrell, S., Wang, D., Li, X., 2005. Origin of sulfur rich oils and H_2S in tertiary lacustrine sections of the Jinxian Sag, Bohai Bay Basin, China. Appl. Geochem. 20, 1427–1444.

Cao, Y., Yuan, G., Li, X., Wang, Y., Xi, K., Wang, X., Jia, Z., Yang, T., 2014. Characteristics and origin of abnormally high porosity zones in buried Paleogene clastic reservoirs in the Shengtuo area, Dongying Sag, East China. Petroleum Sci. 11, 346–362.

Chen, Z., Zhang, J., Wang, L., Zha, M., 2013. Geochemistry of evaporites in lacustrine Basin, Dongying depression, Bohai Bay Basin, China. J. Petroleum Environ. Biotechnol. 4, 1–15.

Chuhan, F., Bjørlykke, K., Lowrey, C.J., 2001. Closed-system burial diagenesis in reservoir sandstones: example from the Garn Formation at Haltenbanken area, offshore Mid-Norway. J. Sediment. Res. 71, 15–26.

Curtis, C.D., 1978. Possible links between sandstone diagenesis and depth-related geochemical reactions occurring in enclosing mudstones. J. Geol. Soc. Lond. 135, 107–117.

Dickson, J.A., 1965. Carbonate identification and genesis as revealed by staining. J. Sediment. Pet. 27, 107–118.

Dong, W., Lin, C.S., Eriksson, K.A., Zhou, X.H., Liu, J.Y., Teng, Y.B., 2011. Depositional systems and sequence architecture of the Oligocene Dongying formation, Liaozhong depression, Bohai Bay Basin, northeast China. AAPG Bull. 95, 1475–1493.

Fayek, M., Harrison, T.M., Grove, M., Mckeegan, K.D., Coath, C.D., Boles, J.R., 2001. In situ stable isotopic evidence for protracted and complex carbonate cementation in a petroleum reservoir, North Coles Levee, San Joaquin Basin, California, USA. J. Sediment. Res. 71, 444–458.

Fisher, J.B., Boles, J.R., 1990. Water-rock interaction in tertiary sandstones, San Joaquin California, USA. Chem. Geol. 82, 83–101.

Folk, R.L., 1974. Petrology of Sedimentary Rocks. Hemphill Press, Texas, 182 pp.

Giles, M.R., de Boer, R.B., 1990. Origin and significance of redistributional secondary porosity. Mar. Pet. Geol. 7, 378–396.

Goldstein, R.H., 2001. Fluid inclusions in sedimentary and diagenetic systems. Lithos 55, 159–193.

Goldstein, R.H., Reynolds, T.J., 1994. Systematics of fluid inclusions in diagenetic minerals. SEPM Short. Course 31, 199.

Guo, X.W., He, S., Liu, K.Y., Song, G.Q., Wang, X.J., Shi, Z.S., 2010. Oil generation as the dominant overpressure mechanism in the Cenozoic Dongying depression, Bohai Bay Basin, China. AAPG Bull. 94, 1859–1881.

Hao, F., Zhang, X., Wang, C., Li, P., Guo, T., Zou, H., Zhu, Y., Liu, J., Cai, Z., 2015. The fate of CO_2 derived from thermochemical sulfate reduction (TSR) and effect of TSR on carbonate porosity and permeability, Sichuan Basin, China. Earth Sci. Rev. 141, 154–177.

Harrison, T.N., 2012. Experimental VNIR reflectance spectroscopy of gypsum dehydration: investigating the gypsum to bassanite transition. Am. Mineral. 97, 598–609.

Hendry, J.P., Wilkinson, M., Fallick, A.E., Haszeldine, R.S., 2000. Ankerite cementation in deeply buried Jurassic sandstone reservoirs of the central North Sea. J. Sediment. Res. 70, 227–239.

Hu, S.B., O'Sullivan, P.B., Raza, A., Kohn, B.P., 2001. Thermal history and tectonic subsidence of the Bohai Basin, northern China: a Cenozoic rifted and local pull-apart basin. Phys. Earth Planet. In. 126, 221–235.

Huang, S.J., Huang, K.K., Lü, J., Lan, Y.F., 2014. The relationship between dolomite textures and their formation temperature: a case study from the Permian-Triassic of the Sichuan Basin and the Lower Paleozoic of the Tarim Basin. Pet. Sci. 11, 39–51.

Iribar, V., Ábalos, B., 2011. The geochemical and isotopic record of evaporite recycling in spas and salterns of the Basque Cantabrian basin. Spain. Appl. Geochem. 26, 1315–1329.

Irwin, H., Curtis, C., Coleman, M., 1977. Isotopic evidence for source of diagenetic carbonates formed during burial of organic-rich sediments. Nature 269, 209–213.

Jiang, S., Henriksen, S., Wang, H., Lu, Y.C., Ren, J.Y., Cai, D.S., Feng, Y.L., Weimer, P., 2013. Sequence-stratigraphic architectures and sand-body distribution in Cenozoic rifted lacustrine basins, east China. AAPG Bull. 97, 1447–1475.

Jordan, G., Astilleros, J.M., 2006. In situ HAFM study of the thermal dehydration on gypsum (010) surfaces. Am. Mineral. 91, 619–627.

Jowett, E.C., Cathles, L.M., Davis, B.W., 1993. Predicting depths of gypsum dehydration in evaporitic sedimentary basins. AAPG Bull. 77, 402–413.

Kantorowicz, J.D., 1985. The origin of authigenic ankerite from the Ninian field, UK North Sea. Nature 315, 214–216.

Lindtke, J., Ziegenbalg, S.B., Brunner, B., Rouchy, J.M., Pierre, C., Peckmann, J., 2011. Authigenesis of native sulphur and dolomite in a lacustrine evaporitic setting (Hellín basin, Late Miocene, SE Spain). Geol. Mag. 148, 655–669.

Liu, C., 1998. Carbon and oxygen isotopic compositions of lacustrine carbonates of the Shahejie formation in the Dongying depression and their paleolimnological significance. Acta Sediment. Sin. 16, 109–114 (In Chinese with English abstract).

Lowenstein, T.K., Hardie, L.A., 1985. Criteria for the recognition of salt-pan evaporites: petrographic and fluid inclusion evidence. Am. J. Sci. 290, 1–42.

Machel, H.G., 2001. Bacterial and thermochemical sulfate reduction in diagenetic settings-old and new insights. Sediment. Geol. 140, 143–175.

Machel, H.G., Buschkuehle, B.E., 2008. Diagenesis of the Devonian southesk-cairn carbonate complex, Alberta, Canada: marine cementation, burial dolomitization, thermochemical sulfate reduction, anhydritization, and squeegee fluid flow. J. Sediment. Res. 78, 366–389.

Major, R.P., Holtz, M.H., 1997. Predicting reservoir quality at the development scale: methods for quantifying remaining hydrocarbon resource in diagenetically complex carbonate reservoirs. In: Kupecz, J.A., Gluyas, J., Bloch, S. (Eds.), Reservoir Quality Prediction in Sandstones and Carbonates, AAPG Memoir,, 69, pp. 231–248.

Morad, S., Ketzer, J.M., Deros, L.F., 2000. Spatial and temporal distribution of diagenetic alterations in siliciclastic rocks: implications for mass transfer in sedimentary basin. Sedimentology 47, 95–120.

Muchez, P., Vanderhaeghen, P., Desouky, H.E., Schneider, J., Boyce, A., Dewaele, S., Cailteux, J., 2008. Anhydrite pseudomorphs and the origin of stratiform Cu-Co ores in the Katangan Copperbelt (Democratic Republic of Congo). Min. Deposita 5, 575–589.

Nollet, S., Hilgers, C., Urai, J., 2005. Sealing of fluid pathways in overpressure cells: a case study from the Buntsandstein in the Lower Saxony Basin (NW Germany). Int. J. Earth Sci. 94, 1039–1055.

Ogawa, Y., Shikazono, N., Ishiyama, D., Sato, H., Mizuta, T., Nakano, T., 2007. Mechanisms for anhydrite and gypsum formation in the Kuroko massive sulfide-sulfate deposits, north Japan. Min. Deposita 42, 219–233.

Ortí, F., Rosell, L., Gibert, L., Moragas, M., Playà, E., Inglès, M., Rouchy, J.M., Calvo, J.P., Gimeno, D., 2014. Evaporite sedimentation in a tectonically active basin: the lacustrine Las Minas Gypsum unit (Late Tortonian, SE Spain). Sediment. Geol. 311, 17–42.

Rahimpour-Bonab, H., Esrafili-Dizaji, B., Tavakoli, V., 2010. Dolomitization and anhydrite precipitation in Permo-Triassic carbonates at the south pars gasfield, offshore Iran: controls on reservoir quality. J. Pet. Geol. 33, 43–66.

Rahman, M.J.J., McCann, T., 2012. Diagenetic history of the Surma group sandstones (Miocene) in the Surma Basin, Bangladesh. J. Asian Earth Sci. 45, 65–78.

Sarg, J.F., 2001. The sequence stratigraphy, sedimentology, and economic importance of evaporite-carbonate transitions: a review. Sediment. Geol. 140, 9–42.

Schenk, P.E., von Bitter, P.H., Matsumoto, R., 1994. Deep-basin/deep-water carbonate-evaporite deposition of a saline giant: Loch Macumber (Visean), Atlantic Canada. Carbonates Evaporites 9, 187–210.

Schorn, A., Neubauer, F., 2014. The structure of the Hallstatt evaporite body (Northern Calcareous Alps, Austria): a compressive diapir superposed by strike-slip shear? J. Struct. Geol. 60, 70–84.

Siriwardane, H., Haljasmaa, I., McLendon, R., Irdi, G., Soong, Y., Bromhal, G., 2009. Influence of carbon dioxide on coal permeability determined by pressure transient methods. Int. J. Coal Geol. 77, 109–118.

Song, G.Q., Jiang, Y.L., Liu, H., Cai, D.M., 2009. Pooling history of cracked gas in middle-deep reservoirs in Lijin-Minfeng areas of the Dongying sag. Nat. Gas. Ind. 29, 14–17 (In Chinese with English Abstract).

Song, M.S., Li, C.L., Zhang, J.L., 2012. Fine division and correlation of conglomerate sedimentary cycles in Yanjia area of Dongying depression. Acta Pet. Sin. 33, 781–788 (in Chinese with English abstract).

Sui, F.G., Cao, Y.C., Liu, H.M., Wang, Y.Z., 2010. Physical properties evolution and hydrocarbon accumulation of Paleogene nearshore subaqueous fan in the eastern north margin of the Dongying depression. Acta Geol. Sin. 84, 247–255 (in Chinese with English abstract).

Taberner, C., Cendón, D.I., Pueyo, J.J., Ayora, C., 2000. The use of environmental markers to distinguish marine vs. continental deposition and to quantify the significance of recycling in evaporite basins. Sediment. Geol. 137, 213–240.

Tangestani, M.H., Validabadi, K., 2014. Mineralogy and geochemistry of alteration induced by hydrocarbon seepage in an evaporite formation: a case study from the Zagros Fold Belt, SW Iran. Appl. Geochem. 41, 189–195.

Tanguay, H.L., Friedman, G.M., 2001. Petrophysical facies of the Ordovician red river formation, Williston Basin, U.S.A. Carbonates Evaporites 16, 71–92.

Topper, R.P.M., Meijer, P.T., 2013. A modeling perspective on spatial and temporal variations in Messinian evaporite deposits. Mar. Geol. 336, 44–60.

Trichet, J., Défarge, C., Tribble, J., Tribble, G., Sansone, F., 2001. Christmas Island lagoonal lakes, models for the deposition of carbonate-evaporite-organic laminated sediments. Sediment. Geol. 140, 177–189.

Tucker, M.E., 1991. Sequence stratigraphy of carbonate-evaporite basins: models and application to the Upper Permian (Zechstein) of northeast England and adjoining North Sea. J. Geol. Soc. Lond. 148, 1019–1036.

Vandeginste, V., Swennen, R., Gleeson, S.A., Ellam, R.M., Osadetz, K., Roure, F., 2009.

Thermochemical sulphate reduction in the upper Devonian cairn formation of the fairholme carbonate complex (South-West Alberta, Canadian Rockies): evidence from fluid inclusions and isotopic data. Sedimentology 56, 439—460.

Wan, N.M., Wang, Y.Z., Cao, Y.C., Song, G.Q., 2010. Overpressured fluid compartment and hydrocarbon accumulation of deep layer of Es4 in the north zone of Minfeng Sag, Dongying Depression. Acta Sediment. Sin. 28, 395—400 (In Chinese with English Abstract).

Wang, Y.Z., Cao, Y.C., Ma, B.B., Liu, H.M., Gao, Y.J., Chen, L., 2014. Mechanism of diagenetic trap formation in nearshore subaqueous fans on steep rift lacustrine basin slopes-A case study from the Shahejie Formation on the north slope of the Minfeng Subsag, Bohai Basin, China. Pet. Sci. 11, 481—494.

Warren, J.K., 2000. Dolomite: occurrence, evolution and economically important associations. Earth Sci. Rev. 52, 1—81.

Warren, J.K., 2006. Evaporites: Sediments, Resources and Hydrocarbons. Springer, Berlin, p. 1019.

Warren, J.K., 2010. Evaporites through time: tectonic, climatic and eustatic controls in marine and nonmarine deposits. Earth Sci. Rev. 98, 217—268.

Worden, R.H., Smalley, P.C., Cross, M.M., 2000. The influence of rock fabric and mineralogy on thermochemical sulfate reduction: Khuff formation, Abu Dhabi. J. Sediment. Res. 70, 1210—1221.

Wright, D.T., 1999. The role of sulphate-reducing bacteria and cyanobacteria in dolomite formation in distal ephemeral lakes of the Coorong region, South Australia. Sediment. Geol. 126, 147—157.

Yuan, G., Gluyas, J., Cao, Y., Oxtoby, N.H., Jia, Z., Wang, Y., Xi, K., Li, X., 2015. Diagenesis and reservoir quality evolution of the Eocene sandstones in the northern Dongying Sag, Bohai Bay Basin, East China. Mar. Pet. Geol. 62, 77—89.

Yuan, J., Wang, Q.Z., 2001. Distribution and generation of deep reservoir secondary pores in Paleogene, Dongying sag. J. Mineral. Pet. 21, 43—47 (in Chinese with English abstract).